

Testing an Alternative Eddy Viscosity Scheme

by

Ginny Anne Marshall

A thesis submitted in partial fulfillment of the requirements for the degree of
Master of Science

Department of Earth and Atmospheric Sciences
University of Alberta
Canada

©Ginny Anne Marshall, 2015

Abstract

The purpose of this thesis is to evaluate the performance of an alternative eddy viscosity scheme proposed by Wilson (2012) for use in single column models of the atmospheric boundary layer (ABL). More popular schemes parameterize eddy viscosity as a function of turbulent kinetic energy, since turbulent mixing should increase as turbulent kinetic energy increases. However, it is an implication of Taylor's (1921) Lagrangian theory of dispersion that time and velocity scales relevant to eddy viscosity are functions of vertical velocity statistics. As such, vertical statistics are seemingly a more sensible choice when parameterizing eddy viscosity; thus, the scheme proposed parameterizes eddy viscosity as a function of vertical velocity variance and an empirical time scale.

In this thesis, the new scheme has been tested against an experiment that was conducted in Kansas in 1999 during the Cooperative Atmosphere-Surface Exchange Study in 1999 (CASES-99) (Poulos et al., 2002). The protocol for the test is identical to that outlined by Svensson et al. (2011) which has been used to compare the performance of various ABL closure models. The test was run for 59 hours and model results were compared to observations, model results from a scheme proposed by Bélair et al. (1999), and results presented by Svensson et al. (2011). Results show that the alternative scheme performs reasonably well, comparable to many schemes presented by Svensson et al. (2011), and no worse than Bélair's scheme, although it may not erode the stable surface inversion fast enough. Modeled 10 m wind speed, turbulent kinetic energy, friction velocity and sensible heat flux show a delayed response to the driving surface warming which is evident in the 3-4 hour lag observed in the increase of these quantities during the transition from the stable morning to the turbulent afternoon. Unfortunately the experiment was performed for only one full diurnal cycle, so it cannot be concluded that the problem lies in the model parameterization; therefore, further testing is required.

Dedication

For Jared, Corbin and Payton.

Acknowledgments

I thank my supervisor, Dr. John Wilson, for his guidance, patience and feedback throughout this M.Sc thesis project. I would also like to thank Drs. Gerhard Reuter and Paul Myers for their suggested thesis edits and feedback. Finally, many thanks to Dr. Mike Flannigan, Dr. Xianli Wang and the Renewable Resources Fire Lab for their support. This research and graduate program was funded by the University of Alberta and by the Natural Sciences and Engineering Research Council of Canada. Data was provided by NCAR/EOL under sponsorship of the National Science Foundation.

Contents

1	Introduction	1
2	The Atmospheric Boundary Layer	4
2.1	Surface layer and Monin-Obukhov similarity theory	5
2.2	Outer layer	8
3	Reynolds-Averaged Navier-Stokes Equations	11
4	Closure Schemes	15
4.1	Zero-order closures	15
4.2	First-order closures	16
4.2.1	K profile schemes	16
4.2.2	Mixing length (Prandtl class) schemes	17
4.3	One-and-a-half order closures	19
4.3.1	l -model closure	20
4.3.2	$k - \epsilon$ model closure	22
4.3.3	$k - l$ model closure	22
4.3.4	$\sigma_w^2 - \tau_w$ model closure	23
4.4	Second- and higher-order closures	24
4.5	Other models	24
5	Methodology	26
5.1	Model inter-comparison study: the second GABLS experiment and its specifications	26
5.2	The $\sigma_w^2 - \tau_w$ model	28
5.2.1	Model equations	28
5.2.2	The surface layer within the model	31
5.2.3	Discretization	32

5.2.4	Grid	33
5.2.5	Initial and boundary conditions	35
5.3	Tower data	39
5.4	Sounding data	41
6	Results	42
6.1	Time series	42
6.2	Vertical profiles	52
7	Discussion	56
8	Further Research	64
9	Conclusion	65
	References	66
	Appendix A Model Surface Layer - Kerang Simulations	71
	Appendix B Model Surface Drag	73
	Appendix C WPL and Schotanus Corrections	74
	Appendix D Monin Obukhov Similarity Theory Profiles	75

List of Tables

5.1	Model grid point height examples where wind speed, temperature and humidity are calculated. Grid points for TKE and vertical velocity variance are located half way between the wind speed, temperature and humidity grid points	35
5.2	Initial conditions for potential temperature and specific humidity as specified by Svensson et al. (2011)	36
5.3	Time series of surface temperature ($^{\circ}\text{C}$) (Svensson et al., 2011) adjusted 2 hours forward in time, where t is time in hours	39
5.4	Variables at given tower height for the CASES-99 experiment provided by UCAR (u, v and w are corrected for sonic tilt). u, v and w are the zonal, meridional and vertical wind speeds (ms^{-1}), T_v is virtual temperature ($^{\circ}\text{C}$), ρ_v is the water vapor density from a Campbell krypton hygrometer (g m^{-3}) and r_c is the CO_2 mixing ratio (mg m^{-3})	40

List of Figures

2.1	Idealized day time and night time ABL profiles; (a) day time wind, temperature and humidity profiles (b) evening wind, temperature and humidity profiles (c) day time vertical flux profiles for wind, temperature and humidity (d) evening vertical flux profiles for wind, temperature and humidity. U denotes scalar wind speed and U' is the departure from the scalar wind speed. Note: the magnitudes of day time and evening heat fluxes are not to the same scale	9
4.1	Air parcel movement in linear environmental wind gradient. Adapted from Stull (1988).	17
5.1	Time series of temperature at 2 m AGL. The solid black line is model output after incorporating a relaxation on eddy viscosity and the dashed line is before relaxation is applied	31
5.2	Uniformly spaced grid control layer for illustrative purposes. N , P and S indicate grid points, and n and s are the upper and lower limits of the control layer . . .	32
6.1	Time series of temperature at 2 m AGL. The black dots indicate Central Tower observations, the solid black line illustrates the $\sigma_w^2 - \tau_w$ model results, the solid gray line shows the Bélair closure results and the dashed-dotted gray line represents the prescribed skin temperature.	43
6.2	Time series of wind at 10 m AGL	44
6.3	Time series of sensible heat flux	45
6.4	Time series of tower averaged friction velocity	46
6.5	Time series of tower averaged stability-dependent drag coefficient	48
6.6	Time series of tower averaged turbulent kinetic energy	49
6.7	Time series of tower averaged vertical velocity variance	50
6.8	Time series of inverse Obukhov length	51
6.9	Potential temperature profiles for October 23, 14:00 LT; 22 hours after initialization	53

6.10	Wind speed profiles for October 23, 14:00 LT; 22 hours after initialization . . .	54
6.11	TKE model profiles for October 23, 14:00 LT; 22 hours after initialization . . .	55
7.1	Near surface potential temperature profiles for the $\sigma_w^2 - \tau_w$ and Bélair schemes on October 23; (a) 08:00 LT (b) 09:00 LT (c) 10:00 LT (d) 11:00 LT (e) 12:00 LT	58
7.2	Potential temperature on October 23 at 18:00 LT	59
7.3	Sensible heat flux time series for the Bélair scheme using two different grids . .	61
7.4	Potential temperature profile for the Bélair scheme using two different grids for October 23,14:00 LT	62
A.1	Surface layer profiles as produced by the model, MOST and observations taken during the Kerang surface layer experiment; (a) Potential temperature (b) Wind speed (c) Specific humidity. Note: the model is forced to fit the observations at a single level, viz. $z=1$ m.	72
D.1	Potential temperature and fitted MO profiles for October 24 02:25 LT; (a) all tower data used to fit MO profiles; $L=9.6$ m and (b) all tower data less than $3L$ used to fit MO profile; $L=6.3$ m	77
D.2	Potential temperature mean measurement and fitted MO profile during unstable stratification for October 23 15:00 LT	78

List of symbols

Subscript 0 denotes surface value unless otherwise noted

Subscripts m , h and w indicate momentum, heat and water vapor

Prime indicates instantaneous fluctuation from the mean quantity

Overbar indicates time averaged quantity

B_i	body forces
C	concentration
C_D	drag coefficient
C_h	heat transfer coefficient
C_w	water vapor transfer coefficient
c_p	specific heat capacity of air
g	gravitational acceleration
E_p	phase change rate
f	Coriolis parameter
H	sensible heat flux
K	eddy viscosity or eddy diffusivity
k	turbulent kinetic energy
k_v	von Karman constant
L	Obukhov length
L_p	latent heat
l	length scale
l_*	reference length scale
l_∞	limiting length scale
N	Brunt-Vaisala frequency
p	atmospheric pressure
Q	specific humidity

Q_*	specific humidity scale
Q_j^*	radiation component
Ri	gradient Richardson number
r	relaxation coefficient
r_c	CO ₂ mixing ratio
S	surface drag
S_c	source term
S_m	stability function
T	temperature
T_*	temperature scale
T_v	virtual temperature
t	time
U	scalar wind speed
u	zonal wind velocity
u_N, u_P, u_S	zonal wind velocity at specified grid points
u_g	geostrophic zonal wind velocity
u_i	velocity vector using tensor notation
u_*	friction velocity
v	meridional wind velocity
v_N, v_P, v_S	meridional wind velocity at specified grid points
v_g	geostrophic meridional wind velocity
w	vertical wind velocity
w_n, w_s	vertical wind velocity at specified grid points
x_i	positional vector in tensor notation
z	height above ground
z_t	height of the model domain
z_0	roughness length

z_*	transformation height coordinate
β	Blackadar constant
γ	empirical constant
δ	height of the boundary layer
δ_{ij}	Kronecker delta tensor
ε	turbulent kinetic energy dissipation
ε_{ijk}	unit tensor
ζ	ratio of height above ground to Obukhov length
η_i	unit vector
θ	potential temperature
θ_*	temperature scale
λ	Blackadar limiting length scale
ν	kinematic viscosity
ν_θ	thermal diffusivity
ν_C	molecular diffusivity for scalar concentration
ρ	air density
ρ_v	water vapor density
σ_u^2	variance of zonal velocity
σ_v^2	variance of meridional velocity
σ_w^2	variance of vertical velocity
τ	shear stress
τ_w	turbulent time scale
$\tau_{w,SL}$	turbulent time scale in the surface layer
τ_∞	limiting time scale
Φ	stability parameter in the Bélair closure scheme
ϕ_m, ϕ_h, ϕ_w	universal Monin-Obukhov similarity theory gradient functions
$\phi_{uu}, \phi_{vv}, \phi_{ww}$	universal Monin-Obukhov similarity theory velocity variance functions

Ψ_m, Ψ_h, Ψ_w universal Monin-Obukhov similarity theory similarity functions
 Ω earth's angular velocity

1 Introduction

Numerical solutions of the non-linear partial differential equations (PDEs) which govern fluid motion (turbulent or laminar), known as the Navier-Stokes equations, are the essential elements of modern numerical weather prediction. These PDEs are derived from Newton's second law and are exact; however, due to their complexity few solutions are known and those that are known are highly specific, i.e., lack the generality to be of any use for weather prediction. As a result, in general one must turn to numerical methods to find approximate solutions.

The motion field within the ABL features co-existing eddies whose size range spans from the largest scales characterized by the depth of the ABL (which can be several hundred meters up to several kilometers in depth) to smaller scales described by Kolmogorov scales, where molecular viscosity is significant. Turbulence (which is chaotic and unsteady and exists on many different scales) plays a key role in the flow. When modeling atmospheric flows it is impossible to obtain solutions that entail motion on such a wide range of length and time scales; often the physics is too complicated to model explicitly, or the exact physics may be unknown. As a result, one must adopt approximations, or parameterizations, and numerical methods must properly parametrize a wide range of eddy scales to provide accurate solutions. In practice, motion in the ABL is viewed as being governed by the Reynolds-averaged Navier-Stokes equations (RANS), which govern the *average* velocity (and temperature, etc.) and are derived by applying an averaging operator to the Navier-Stokes equations. The set of Reynolds equations, however, are “unclosed” (there are more unknowns than there are equations) and they must be “closed” by adopting further *empirical* relationships.

The focus of this research is to evaluate a parameterization scheme which approximates turbulent fluxes in the horizontally homogeneous ABL¹ by representing them as the product of a mixing coefficient (the “eddy diffusivity” or “eddy viscosity”, K) and the mean spatial gradient of the property being transported. This method, generically known as K -theory or as “first-order closure”, approximates turbulent convective processes as though they are diffusive processes.

¹Within the mixed layer above the surface layer.

The challenge numerical modelers face is how to properly represent the eddy viscosity, which accounts for turbulent complexities (Holt and Raman, 1988). Since Reynolds first recognized the importance of eddy fluxes of momentum and other properties, there have been many proposed eddy viscosity schemes, from constant (i.e., height-independent) values of K to approximating it by three (or more) equation schemes involving three separate transport equations governing statistical properties that are subject to advection, diffusion and production/destruction. Many of these schemes incorporate turbulent kinetic energy (TKE, k), where TKE is defined as

$$k = \frac{1}{2} (\sigma_u^2 + \sigma_v^2 + \sigma_w^2), \quad (1.1)$$

and σ_u^2 , σ_v^2 and σ_w^2 are respectively the zonal, meridional and vertical velocity variances (a more comprehensive discussion on eddy viscosity schemes is featured in Section 4). While parameterizing eddy viscosity for vertical fluxes (which is required in single column models) by way of TKE may at first seem logical, the length and velocity scales needed to parametrize this eddy viscosity are governed by *vertical* statistics of the fluid motion (Taylor, 1921), whereas TKE is a three-dimensional quantity. By incorporating TKE into eddy viscosity, one is incorporating horizontal velocity statistics when what is actually relevant is the vertical velocity statistics. Motivated by this inconsistency, Wilson (2012) adopts an alternative scheme, where eddy viscosity is parametrized through the standard deviation of vertical velocity and an associated time scale.

The alternative scheme has been previously tested against the Wangara day 33 ABL experiment observations (Clarke et al., 1971; Hess et al., 1981) and against a version of the Bélair et al. (1999) scheme. It performed adequately (Wilson, 2012), however, it remains relatively untested otherwise. The focus of this thesis is to test the scheme using the second GEWEX (Global Energy and Water cycle EXperiment) Atmospheric Boundary Layer Study (GABLS), a study developed by Svensson et al. (2011), in an effort to evaluate the closure scheme further and gain insight into its utility. The study was developed using observations taken from the CASES-99 experiment, and its purpose is to allow the evaluation of many different closure schemes by providing simple initial conditions, boundary conditions and model forcing in order to reduce

(or ideally eliminate) complex numerical processes (such as the implementation of radiation schemes) which may hinder a simple comparison of model closure performance. After the test is completed, the results are easily compared against experiment observations and model output produced by schemes currently used in research and operational models as found in Svensson et al. (2011). This thesis research presents the results of the second GABLS experiment as implemented by the alternative scheme, and adds further insight into model performance.

2 The Atmospheric Boundary Layer

As previously discussed, the atmospheric boundary layer features turbulent eddies of varying size from (of the order of) the depth of the boundary layer to scales where molecular viscosity is significant. This boundary layer is not static and its depth and other characteristics change throughout the diurnal cycle. After sunrise when the surface is heated by solar radiation, turbulence (via convection in the statically unstable atmosphere) helps to create a well mixed ABL whose depth may reach 1-2 km. This well mixed layer is very close to adiabatic, while near surface conditions are often super-adiabatic, and the uppermost layer is characterized by a capping inversion. As the surface begins to cool (beginning shortly before sunset), a surface inversion will develop and the well mixed layer above the surface layer transitions to a residual layer as turbulence decays. As the night progresses and surface layer cooling continues (due to divergence of the sensible heat and radiative fluxes; Arya 2005), the stable layer at the surface grows in depth until shortly after sunrise when surface heating begins to erode the surface inversion and the diurnal cycle for the atmospheric boundary layer begins again.

The ABL can be subdivided into two layers: the inner (surface) and outer layers. The flow within the outer layer is little influenced by surface characteristics and is subject to the Coriolis effect (Garratt, 1992); due to the effects of the Coriolis force, the outer layer is often termed the 'Ekman' layer. The outer layer is often characterized by little wind shear, whereas the inner layer is strongly sheared as surface characteristics (i.e., friction) play an important role. The inner layer is little influenced by the Coriolis effect, therefore the Coriolis force is often excluded when representing the surface layer and wind direction is normally assumed height independent. Below the inner layer and very near the surface is a shallow region known as the roughness sublayer. In this region flow is strongly affected by individual roughness elements, such as plants and buildings, etc.

2.1 Surface layer and Monin-Obukhov similarity theory

The surface layer, also known as the constant flux layer, is the layer of the ABL closest to the ground. Typically the surface layer is considered to be the lowest 10% of the ABL and over that shallow distance it is considered usual that the mean vertical fluxes (of heat, momentum, etc.) would vary by less than approximately 10% of their surface values (Stull, 1988). It is within this layer that the Monin-Obukhov Similarity Theory (MOST) is valid. MOST is founded on the basis that turbulence within the atmospheric surface layer is dependent only on the parameters $\overline{u'w'}$, $\overline{w'\theta'}$, z , and $\frac{g}{\theta_0}$, where $\overline{u'w'}$ is the turbulent momentum flux², $\overline{w'\theta'}$ is the vertical heat flux at the surface, z is height above the ground, $\frac{g}{\theta_0}$ is the ratio of gravity to surface temperature (in Kelvin), u' and w' indicate instantaneous fluctuations about the mean horizontal and vertical velocity respectively, and θ' is the instantaneous fluctuation about the mean temperature. These parameters are used to normalize the flow variables, and all normalized flow variables are functions of $\frac{z}{L}$, a buoyancy parameter (Arya, 1988), which is the ratio of height above ground to the Obukhov length, a stability parameter. The Obukhov length is

$$L = \frac{-\theta_0 u_*^3}{k_v g \overline{w'\theta'}}, \quad (2.1)$$

where θ_0 is the mean potential temperature at the surface, k_v is the von Karman constant ($k_v = 0.4$) and u_* is the friction velocity which is generally defined as

$$u_*^4 = \overline{u'w'^2} + \overline{v'w'^2}. \quad (2.2)$$

The Obukhov length represents the height where the rates of production of TKE by shear and buoyancy forces are approximately the same (Apsley and Castro, 1997). These assumptions are only valid where $z_0 \ll z \ll \delta$ (z_0 is the roughness length and δ is the height of the ABL above ground level), for horizontally homogeneous flow where turbulent fluxes are almost height independent, and viscosity is insignificant when compared to turbulent exchange (Arya, 1988).

²It is here assumed the coordinate system is rotated such that $\overline{v'w'} = 0$.

If the x -axis is rotated parallel to the direction of wind, the non-dimensionalized mean wind, mean potential temperature and mean specific humidity profiles according to MOST are:

$$\frac{k_v z}{u_*} \frac{\partial U}{\partial z} = \phi_m(\zeta), \quad (2.3)$$

$$\frac{k_v z}{\theta_*} \frac{\partial \theta}{\partial z} = \phi_h(\zeta) \quad (2.4)$$

and

$$\frac{k_v z}{Q_*} \frac{\partial Q}{\partial z} = \phi_w(\zeta) \quad (2.5)$$

where U , θ and Q are the mean wind speed, mean potential temperature and mean specific humidity, ζ is $\frac{z}{L}$, and $\phi_m(\zeta)$, $\phi_h(\zeta)$ and $\phi_w(\zeta)$ are dimensionless gradient functions for wind, potential temperature and specific humidity. The scaling parameters u_* (henceforth friction velocity), θ_* and Q_* are specified as:

$$u_* = \left(\frac{\tau_0}{\rho} \right)^{\frac{1}{2}}, \quad (2.6)$$

$$\theta_* = - \frac{H_0}{\rho c_p u_*} \quad (2.7)$$

and

$$Q_* = - \frac{E_0}{\rho u_*}. \quad (2.8)$$

In these equations τ_0 is the surface shear stress, H_0 is the surface sensible heat flux density, c_p is the specific heat capacity of air, ρ is air density and E_0 is the surface vapor flux density. In the modeling context the surface fluxes are often parameterized by bulk transfer formulae, viz.,

$$\tau_0 = \rho C_D U^2, \quad (2.9)$$

$$H_0 = -\rho c_p C_h U (\theta - \theta_0) \quad (2.10)$$

and

$$E_0 = -\rho C_w U (Q - Q_0). \quad (2.11)$$

where C_D is a drag coefficient and C_h and C_w are analogous heat and water vapor transfer coefficients.

The dimensionless gradient functions seen in Equations 2.3-2.5 are empirically derived and most often have the form

$$\phi_m = \begin{cases} (1 - \gamma_1 \zeta)^{-n} & \text{if } L < 0 \\ 1 + \gamma_2 \zeta & \text{if } L \geq 0 \end{cases} \quad (2.12)$$

and in some formulations

$$\begin{aligned} \phi_m^2 &= \phi_h = \phi_w & \text{if } L < 0 \\ \phi_m &= \phi_h = \phi_w & \text{if } L \geq 0 \end{aligned} \quad (2.13)$$

where n is often specified as (but not limited to) 1/2, 1/3 or 1/4, and γ_1 and γ_2 are constants determined empirically (Arya, 1988). The Obukhov length varies from $-\infty$ to $+\infty$ with infinite values indicating neutral atmospheric conditions; negative values, unstable conditions and positive values, stable conditions. Thus, neutral conditions result in $\zeta = 0$ and by design as ζ approaches 0, the dimensionless similarity functions approach 1. For the purposes of this research, the gradient functions are specified according to Dyer and Bradley (1982) (see Section 5.2.1).

Within the surface layer, one can calculate wind, potential temperature and specific humidity via the integration of Equations 2.3-2.5, such that

$$U = \frac{u_*}{k_v} \left[\ln \left(\frac{z}{z_0} \right) - \Psi_m(\zeta) \right], \quad (2.14)$$

$$\theta - \theta_0 = \frac{\theta^*}{k_v} \left[\ln \left(\frac{z}{z_0} \right) - \psi_h(\zeta) \right] \quad (2.15)$$

and

$$Q - Q_0 = \frac{Q^*}{k_v} \left[\ln \left(\frac{z}{z_0} \right) - \psi_w(\zeta) \right] \quad (2.16)$$

where ψ_m , ψ_h and ψ_w are similarity functions specified as (taking the momentum similarity function for example)

$$\psi_m(\zeta) = \int_{\frac{z_0}{L}}^{\frac{z}{L}} \frac{1}{\zeta'} [1 - \phi_m(\zeta')] d\zeta' \quad (2.17)$$

as shown by Blackadar (1997).

2.2 Outer layer

The outer layer is the region above the surface layer which spans approximately 90% of the entire ABL depth. As seen in Figures 2.1a-2.1d, the outer layer experiences significant diurnal variations. Day time surface heating promotes a turbulent well mixed layer, while night time cooling results in a ground based inversion which encloses (or perhaps constitutes) the surface layer; this inversion is sometimes referred to as a nocturnal boundary layer (NBL). Unlike the surface layer, turbulent fluxes are not constant with height; however, by day (assuming strong mixing), wind speed, potential temperature, and humidity are nearly height independent.

The outer layer variables are not calculated using similarity theory and instead unknown quantities are calculated by Reynolds averaging and parameterizing the equations for the conservation of momentum, heat, mass and scalar quantities which are respectively (before Reynolds averaging and under the Boussinesq approximation)

$$\frac{\partial u_i}{\partial t} + u_j \frac{\partial u_i}{\partial x_j} = \delta_{i3} g \frac{\theta'}{\theta_0} - \frac{1}{\rho_0} \frac{\partial p'}{\partial x_i} + f \varepsilon_{ij3} u_j + \nu \frac{\partial^2 u_i}{\partial x_j^2}, \quad (2.18)$$

$$\frac{\partial \theta}{\partial t} + u_j \frac{\partial \theta}{\partial x_j} = \nu_\theta \frac{\partial^2 \theta}{\partial x_j^2} - \frac{1}{\rho c_p} \frac{\partial Q_j^*}{\partial x_j} - \frac{L_p E_p}{\rho c_p} \quad (2.19)$$

$$\frac{\partial u_j}{\partial x_j} = 0. \quad (2.20)$$

and

$$\frac{\partial C}{\partial t} + u_j \frac{\partial C}{\partial x_j} = \nu_C \frac{\partial^2 C}{\partial x_j^2} + S_C. \quad (2.21)$$

In these equations u_i is the velocity vector, t is time, x_i is a position vector, δ_{ij} is the Kronecker delta, g is the gravitational acceleration, f is the Coriolis parameter, ϵ_{ijk} is the alternating unit

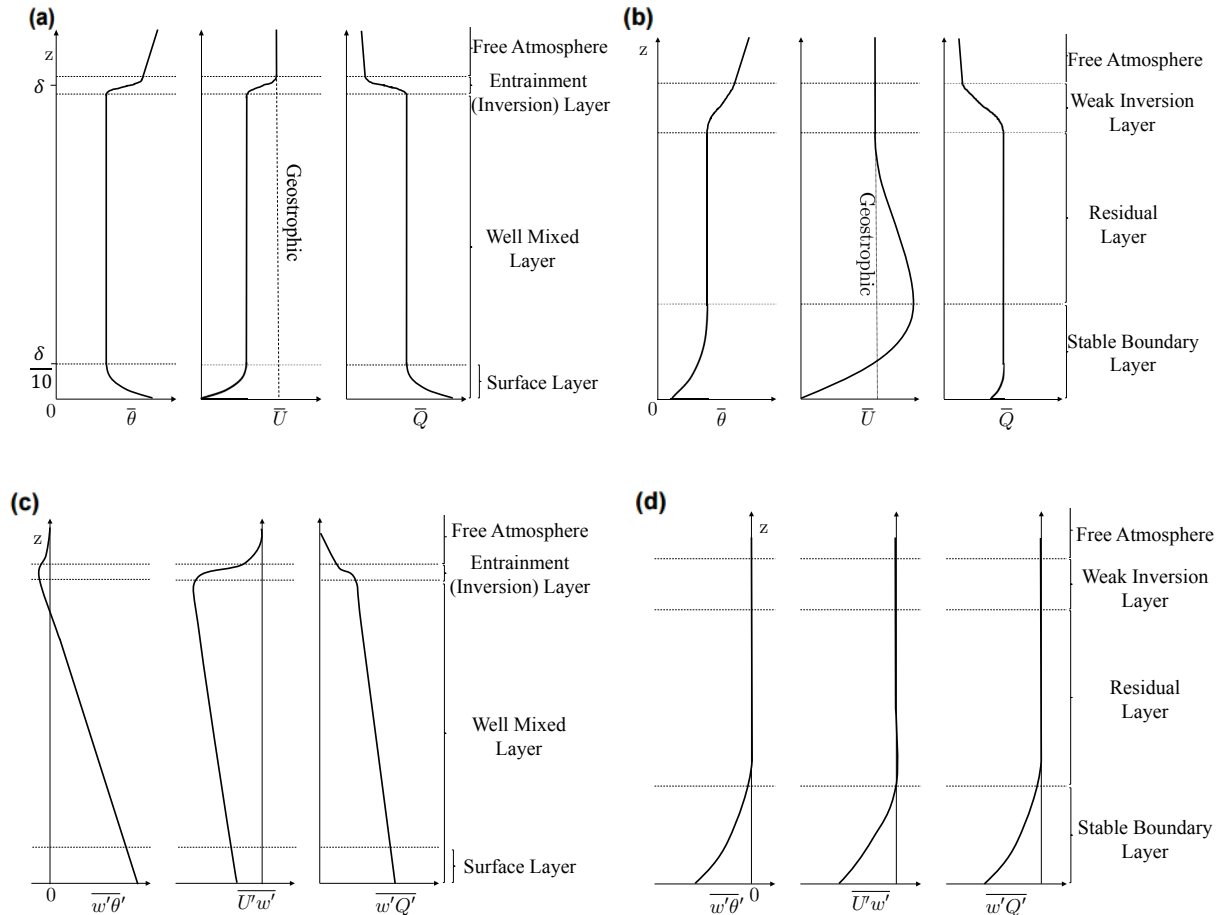


Figure 2.1: Idealized day time and night time ABL profiles; (a) day time wind, temperature and humidity profiles (b) evening wind, temperature and humidity profiles (c) day time vertical flux profiles for wind, temperature and humidity (d) evening vertical flux profiles for wind, temperature and humidity. U denotes scalar wind speed and U' is the departure from the scalar wind speed. Adapted from Stull (1988). Note: the magnitudes of day time and evening heat fluxes are not to the same scale

tensor, p' and θ' are pressure and temperature departures from an adiabatic and hydrostatic reference state, ν is kinematic viscosity, ν_θ is a molecular thermal diffusivity, Q_j^* is a radiation component, L_p is latent heat, E_p is phase change rate, C is a scalar quantity (concentration), ν_C is the molecular diffusivity for the scalar quantity and S_C is a source term. In order to numerically calculate solutions to these equations, as mentioned above, one must apply Reynolds-Averaging and take further steps to parameterize the resultant unclosed equations. This process is described in the following two sections.

3 Reynolds-Averaged Navier-Stokes Equations

As previously discussed, the Navier-Stokes equations which govern fluid motion are complex and general solutions are unknown. Worse yet the Reynolds equations, which are the basis for a rational decomposition into “resolved” and “unresolved” components of the motion, not only inherit the complexity of the Navier-Stokes equations, but they are also unclosed. There are several methods employed to address the closure problem and model the unresolved turbulent quantities ranging from a simple zero order approximation, where the unknowns are directly parametrized, to higher order closure schemes, where triple or even quadruple order moments (fluctuations about the mean flow variable) are parametrized (Stull, 1988). In operational numerical weather prediction models the most common method is closing the unclosed equations via first order closure (i.e., K -theory), which (more or less by analogy to molecular fluxes) approximates second order correlations (or second order moments) through the product of the mean property gradient and a mixing coefficient.

Reynolds-averaging introduces a time or space averaged quantity and a deviation from that average for all flow variables such that generically, i.e., for an arbitrary variable a ,

$$a = \bar{a} + a'. \quad (3.1)$$

These Reynolds-averaged quantities are introduced into the Navier-Stokes equations (for an incompressible flow under the Boussinesq approximation³),

$$\frac{\partial u_i}{\partial t} + u_j \frac{\partial u_i}{\partial x_j} = B_i - \frac{1}{\rho_0} \frac{\partial p'}{\partial x_i} + \nu \frac{\partial^2 u_i}{\partial x_j^2}, \quad (3.2)$$

where B_i represents body forces (such as gravitational and Coriolis forces, etc.; see Equation 2.18). The application of Reynolds-averaging rules to Equation 3.2 (after the appropriate Reynolds-averaged quantity has been applied) results in a new equation,

³This allows us to neglect density differences, except those multiplied by gravitational acceleration.

$$\frac{\partial \bar{u}_i}{\partial t} + \frac{\partial}{\partial x_j} \left(\bar{u}_i \bar{u}_j + \overline{u'_i u'_j} \right) = \bar{B}_i - \frac{1}{\rho_0} \frac{\partial \bar{p}}{\partial x_i} + \mathbf{v} \frac{\partial^2 \bar{u}_i}{\partial x_j^2}, \quad (3.3)$$

which contains new variables, in this case $\overline{u'_i u'_j}$, known as second moment terms, covariances or fluxes. These fluxes transport momentum ($\overline{u'_i u'_j}$), or, in terms of heat and mass transfer (which would be derived from Equations 2.19 and 2.21), they transport heat ($\overline{u'_i \theta'}$) and moisture ($\overline{u'_i Q'}$), where Q' is the instantaneous deviation from mean specific humidity, and the divergence of these terms contributes to changes in the mean concentration. In order to solve for these covariances, one may develop additional equations such as,

$$\begin{aligned} \frac{\partial \overline{u'_i u'_k}}{\partial t} + \bar{u}_j \frac{\partial \overline{u'_i u'_k}}{\partial x_j} = & -\overline{u'_k u'_j} \frac{\partial \bar{u}_i}{\partial x_j} - \overline{u'_i u'_j} \frac{\partial \bar{u}_k}{\partial x_j} - \frac{\partial \overline{u'_i u'_j u'_k}}{\partial x_j} + \frac{g}{\theta_v} \left(\overline{u'_i \theta'_v} \delta_{3k} + \overline{u'_k \theta'_v} \delta_{3i} \right) \\ & - 2\Omega \eta_j \left(\epsilon_{ijl} \overline{u'_k u'_l} + \epsilon_{kjl} \overline{u'_i u'_l} \right) - \frac{1}{\rho} \left[\overline{u'_k \frac{\partial p'}{\partial x_i}} + \overline{u'_i \frac{\partial p'}{\partial x_k}} \right] + \mathbf{v} \left[\overline{u'_k \frac{\partial^2 u'_i}{\partial x_j^2}} + \overline{u'_i \frac{\partial^2 u'_k}{\partial x_j^2}} \right] \end{aligned} \quad (3.4)$$

as illustrated in Garratt (1992), where η_j is the component of the unit vector parallel to the axis of rotation and Ω is the magnitude of the earth's angular velocity; however, this introduces third order moments, which are also unknown. By again solving for the additional terms one introduces further terms and further complexity. As discussed by Stull (1988) (illustrated in his Table 6-1), solving the prognostic equation (of momentum only) for a second order moment requires 6 equations with 10 unknowns, and a prognostic equation for a third order moment requires 10 equations and 15 unknowns. In the interest of computational efficiency, capabilities, and accuracy, the prognostic equations for the mean quantity are normally retained (e.g., Equation 3.3) and the second order terms are parameterized closing the set of equations and allowing one to solve them.

Assuming the flow is horizontally homogeneous and neglecting viscous effects⁴, Equation 3.3 for the mean zonal wind, \bar{u} , (as an example) simplifies to

⁴ABL flow is most often characterized by a high Reynolds number, allowing us to neglect viscous effects.

$$\frac{\partial \bar{u}}{\partial t} = -\frac{\partial \overline{u'w'}}{\partial z} - \frac{\partial \bar{u}\bar{w}}{\partial z} + f(\bar{v} - v_g), \quad (3.5)$$

where the covariance $\overline{u'w'}$ is an unknown Reynolds stress (or more specifically, a (kinematic) turbulent momentum flux density), \bar{w} is the mean vertical velocity, \bar{v} is the mean meridional wind speed and v_g represents the meridional geostrophic component of the wind. As previously discussed the mean momentum flux can then subsequently be parametrized via K -theory. K -theory suggests that in the horizontally homogeneous case the momentum fluxes can be approximated (for instance) as

$$\overline{u'w'} = -K \frac{\partial \bar{u}}{\partial z}, \quad (3.6)$$

where K [$\text{m}^2 \text{s}^{-1}$] is the eddy viscosity⁵ or eddy diffusivity (in the case of scalar transport) and is (dimensionally) the product of a velocity scale and a length scale. This approximation assumes that momentum flows down the gradient in mean velocity, and represents the unknown covariances as functions of known flow quantities. The underlying concept is that turbulent convective processes can be modeled like diffusive processes, which is incorrect in reality, but it can provide realistic solutions in simple flows. Substituting Equation 3.6 into Equation 3.5 gives a parametrized governing equation that can be modeled numerically,

$$\frac{\partial \bar{u}}{\partial t} = \frac{\partial}{\partial z} \left[K \frac{\partial \bar{u}}{\partial z} \right] - \frac{\partial \bar{u}\bar{w}}{\partial z} + f(\bar{v} - v_g), \quad (3.7)$$

where, in this case, Equation 3.7 is coupled to a similar equation for $\partial \bar{v} / \partial t$. The Reynolds-averaged prognostic equations for potential temperature, humidity and scalar variables are also developed using the methods described above, although it should be noted that the eddy viscosity or diffusivity contained in each of these equations (as well as the momentum equation) cannot always be assumed universally equivalent.

⁵Which (at a minimum) must be regarded as being a function of distance z from ground and of the boundary layer stability.

Despite the stated assumption of horizontal homogeneity, the mean vertical velocity, \bar{w} , has been retained in Equations 3.5 and 3.7. This is because the thesis work presented here includes model simulations partially driven by large scale subsidence; thus $\bar{w} \neq 0$.

4 Closure Schemes

While it has been historically speculated that higher order closures⁶ will provide the most realistic results, the eddy viscosity method of turbulent closure is still widely used for research and operational forecasting purposes. For example, the Global Environmental Multiscale Model (GEM), the operational forecasting model used by Environment Canada, employs K -closure in its model physics package (Mailhot et al., 1998a), and similarly first order turbulence closure is also incorporated into the European Centre for Medium-Range Weather Forecasts (ECMWF) model (Thomkins et al., 2004). Higher order closure schemes involve solving more equations and thus require significantly more computing power than lower order schemes. They will not necessarily provide more accurate solutions (Hess and Garratt, 2002), and as discussed by Alfonsi (2009), higher order schemes are not universally valid, therefore they must be tuned to specific cases. It is worth noting, too, that numerical weather prediction models usually compute only the *vertical* transport by subgrid scales of motion, and do so assuming the process is locally horizontally homogeneous, i.e., lateral coupling is neglected. Thus, these calculations treat each column of grid points as being isolated from neighboring columns.

As there is a wide variety of closure schemes available, this section will provide an overview of common local closure schemes and follows the organization and grouping of schemes similar to that found in Holt and Raman's (1988) literature review. While there are many schemes available, here the focus will remain on first and one-and-a-half order schemes.

4.1 Zero-order closures

Similarity theories, or zero-order closures, are the simplest closures as they do not retain any of the prognostic equations and do not model turbulence explicitly. They are built assuming that flows within a given scenario all exhibit the same behavior when scaled appropriately. A classic example is the Monin Obukhov Similarity Theory (MOST) which is commonly applied

⁶That is to say, introduction of simplified transport equations (resolving advective and turbulent transport, production and destruction) for moments such as $\overline{u'w'}$.

in atmospheric surface layer flows and is discussed in greater detail in Section 2.1.

4.2 First-order closures

First order closures are the most common type of closure. This class of closure is founded upon the parameterization of turbulent fluxes (or second order moments) as seen, for example, in Equation 3.6, and retains prognostic equations for the mean variables only (e.g., wind velocity, potential temperature and humidity; see Equations 5.2, 5.3, 5.6 and 5.7). This closure, also known as K -closure, assumes that the turbulent quantities flow down the mean property gradient and that the unknown quantities (typically covariances) can be modeled using the known mean quantities as discussed in Section 3. In their review of first-order closure schemes, Holt and Raman (1988) differentiate between two classes of first-order closure schemes: schemes that incorporate a mixing length in the parameterization for eddy viscosity (mixing length schemes) and those that do not (K profile schemes).

4.2.1 K profile schemes

Among all first-order closure schemes, this class of schemes is the simplest as it does not incorporate a mixing length and simply assigns a profile for K . A classic example of a constant K profile is the Ekman spiral (Ekman, 1905). This simple scheme cannot provide general solutions as eddy viscosity is time and height dependent and Ekman's solutions are based on a horizontally homogeneous, steady state, neutral, barotropic atmosphere with no subsidence (Stull, 1988). Recent work has been done (Marlatt et al., 2012) on K -profiles in the Ekman layer by testing O'Brien's (1970) cubic polynomial profile for eddy diffusivity.

Since the atmosphere is most often not neutral, nor barotropic, prescribing a profile for K as a function of height, stability, gradients etc. will provide a more accurate solution in typical atmospheric conditions. As discussed by Holt and Raman (1988) these schemes are more realistic than constant profiles and are functions of quantities that are easily measured. However, the measured quantities may not be representative of turbulent flow and thus will not

necessarily provide the most realistic solutions when compared with other schemes.

4.2.2 Mixing length (Prandtl class) schemes

A common class of first order closures is the Prandtl class of closures which require a mixing length to parameterize K . Following Stull's (1988) derivation based on Prandtl's arguments,

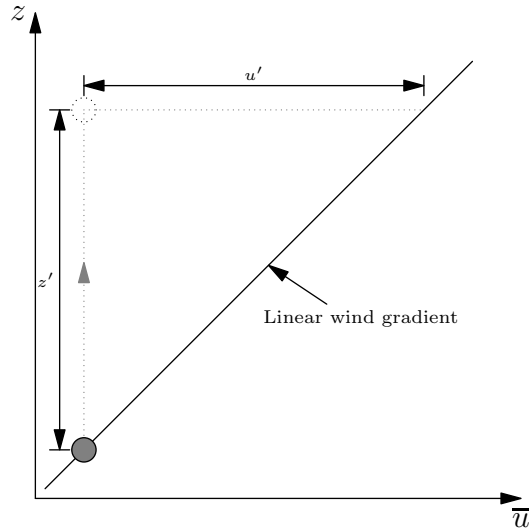


Figure 4.1: Air parcel movement in linear environmental wind gradient. Adapted from Stull (1988).

in a neutral environment if turbulence moves a parcel a distance z' in the vertical direction (see Figure 4.1) and if the parcel retains “its own” initial velocity, the parcel's zonal velocity (as an example) will differ from that of its new environment by

$$u' = - \left(\frac{\partial \bar{u}}{\partial z} \right) z'. \quad (4.1)$$

Since upward motion requires vertical velocity, and assuming vertical and zonal velocities are proportional, then $w' = cu'$, where c is a constant, and thus

$$w' = c \left| \frac{\partial \bar{u}}{\partial z} \right| z'. \quad (4.2)$$

Following a similar argument for an arbitrary variable (e.g., humidity as used by Stull 1988),

one finds the vertical flux of the arbitrary variable a (after averaging) to be

$$\overline{a'w'} = -\overline{cz'^2} \left| \frac{\partial \bar{u}}{\partial z} \right| \frac{\partial \bar{a}}{\partial z}. \quad (4.3)$$

This is directly related to eddy viscosity K , if z' is taken as a length scale l , as

$$K = l^2 \left| \frac{\partial \bar{u}}{\partial z} \right| \quad (4.4)$$

and thus, similar to Equation 3.6,

$$\overline{a'w'} = -K \frac{\partial \bar{a}}{\partial z}. \quad (4.5)$$

Equations 4.2 and 4.3 should not be taken literally and are presented only as a plausible argument for the derivation of Equations 4.4 and 4.5.

Later, Blackadar (1962) developed his well known mixing length profile for the ABL,

$$l = \frac{k_v z}{1 + \frac{k_v z}{\lambda}}, \quad (4.6)$$

where λ is the free atmosphere value of l which Blackadar prescribed as $\lambda = 0.00027 \frac{U_g}{f}$ (it is however meaningless to think in terms of a fixed and precise value of this limiting length scale). He argues that aloft the mixing length approaches a maximum value, however near the surface it approximately varies linearly with $k_v z$. More recent work by Peña et al. (2010) relates the mixing length to turbulent length scales for a range of stability via vertical velocity spectrum and turbulence spectral models. Hess and Garratt (2002) compared results from several mixing length schemes to higher order schemes ($k - \epsilon$ and $k - l$ type schemes, see Sections 4.3.2 and 4.3.3) in a neutral, barotropic ABL and found the simpler mixing-length models performed well. However, as discussed by Stull (1988), this class of schemes is limited in its determination of eddy viscosity, as equations such as or similar to Equation 4.2 are most often valid only in neutral stratification.

4.3 One-and-a-half order closures

This class of closure is arguably the most common type of closure used today. This order of closure requires all the prognostic equations from the first-order class, however, it also requires additional prognostic equations, such as the prognostic TKE equation, which are needed in the parameterization of eddy viscosity. This addition, while adding complexity, is logical, as one would expect eddy viscosity to vanish as turbulence vanishes. This order of closure performs generally better than first-order closure, as additional equations, therefore additional physics, are incorporated into the solutions. As previously mentioned, the first-order mixing-length scheme is valid only in neutral conditions; however, by adding the prognostic equation for TKE (in this case the simplified horizontally homogeneous TKE equation),

$$\frac{\partial k}{\partial t} = -\overline{u'w'}\frac{\partial \bar{u}}{\partial z} - \overline{v'w'}\frac{\partial \bar{v}}{\partial z} + \frac{g}{\theta_0}\overline{w'\theta'} - \frac{\partial}{\partial z}\overline{w'\left(\frac{p'}{\rho_0} + \frac{u'^2 + v'^2 + w'^2}{2}\right)} - \varepsilon, \quad (4.7)$$

one is incorporating terms such as shear and buoyant production, transport and dissipation of TKE (on the right hand side of the Equation respectively) which provide more realistic solutions and the solutions are useful in non-neutral atmospheric conditions. The Kolmogorov parameterization for the TKE dissipation rate is

$$\varepsilon = c_\varepsilon \frac{k^{\frac{3}{2}}}{l_\varepsilon}, \quad (4.8)$$

where c_ε is a constant and l_ε is TKE dissipation length scale. As discussed by Holt and Raman (1988), the one-and-a-half order TKE closure schemes can be subdivided into the l -model, $k - \varepsilon$ model and $k - l$ model schemes. For the purpose of completeness, this literature review will also include a discussion on an additional one-and-a-half order scheme, the $\sigma_w^2 - \tau_w$ scheme (Wilson, 2012) which is the scheme tested in this research.

4.3.1 *l*-model closure

The *l*-Model assigns eddy viscosity as

$$K = clk^{\frac{1}{2}} \quad (4.9)$$

where *l* is a length scale that can be determined either prognostically or diagnostically and *c* is a constant. This closure type is rooted in the Prandtl-Kolmogorov hypothesis (Monin and Yaglom 1971; Pope 2000) and is known as a one equation closure, as it requires an additional prognostic equation for TKE only. Both Prandtl and Kolmogorov suggested that it is appropriate to express a velocity scale as a function of TKE, and thus eddy viscosity as a function of TKE and a length scale giving rise to the *l*-model closure.

Diagnostic determination of the length scale in the most simple models is via Blackadar's (1962) mixing length (Equation 4.6). A well known scheme presented by Therry and Lacarrère (1983) and which was modified by Bougeault and Lacarrere (1989) can be found in the Advanced Research version of the Weather Research and Forecasting Model (ARW WRF) among the optional closures. In this scheme the length scale for TKE dissipation is distinguished from the mixing length scale. TKE dissipation is modeled using the Kolmogorov parameterization (Equation 4.8) where the the length scales are related to the distance a parcel will travel (up and down) before buoyancy stops its movement. Another well known scheme originally developed by Mailhot and Benoit (1982) was further developed by Benoit et al. (1989) and Bélair et al. (1999) and a version is currently used in the GEM model in Canada (Mailhot et al., 1998a; Côté et al., 1998). Both versions of the above mixing length formulations (Bougeault and Lacarrere 1989 and Bélair et al. 1999) can be compared in Bélair et al.'s (1999) study in which local and non-local mixing lengths are used to model two cases from the Montreal-96 Experiment on Regional Mixing and Ozone (MERMOSZ; Mailhot et al. 1998b).

Focusing on the Bélair scheme specifically, Bélair et al. (1999) determines eddy viscosity to

be

$$K = c_\alpha l k^{\frac{1}{2}} \quad (4.10)$$

where c_α is a constant, l is a mixing length that is determined as

$$l = \frac{l_n}{\Phi_m}, \quad (4.11)$$

and TKE is modeled as

$$\frac{\partial k}{\partial t} = K \left[\left(\frac{\partial \bar{u}}{\partial z} \right)^2 + \left(\frac{\partial \bar{v}}{\partial z} \right)^2 \right] - \frac{g}{\theta_v} K \frac{\partial \bar{\theta}_v}{\partial z} + \frac{\partial}{\partial z} \left(K \frac{\partial k}{\partial z} \right) - c \frac{k^{\frac{3}{2}}}{l_\epsilon}. \quad (4.12)$$

l_n is a neutral mixing length, Φ_m is a stability parameter (which is a function of the local gradient Richardson number, Ri) and l_ϵ is a dissipation length scale. These are respectively determined to be

$$l_n = \frac{1}{\frac{1}{k_{vz}} + \frac{1}{200}}, \quad (4.13)$$

$$\Phi_m = \begin{cases} (1 - 40Ri)^{-\frac{1}{6}} & \text{if } Ri < 0 \\ (1 + 12Ri) & \text{if } Ri > 0 \end{cases} \quad (4.14)$$

and

$$l_\epsilon = l_n. \quad (4.15)$$

As this is a well known and tested scheme, we have also included it our results for comparison in Section 6. Please note, however, that this scheme has generally been implemented with the coarse resolution that characterizes an operational model, whereas here it is implemented with high resolution (see Section 5.2.4).

4.3.2 $k - \varepsilon$ model closure

The $k - \varepsilon$ model assigns eddy viscosity as

$$K = c \frac{k^2}{\varepsilon}. \quad (4.16)$$

This model is known as a two equation closure model, as it requires a prognostic equation not only for TKE (see Equation 4.7), but also for TKE dissipation rate. The latter is typically formulated as

$$\frac{\partial \varepsilon}{\partial t} = c_3 \frac{\varepsilon}{k} \left(-\overline{u'w'} \frac{\partial \bar{u}}{\partial z} - \overline{v'w'} \frac{\partial \bar{v}}{\partial z} + \frac{g}{\theta} \overline{w'\theta'} \right) - c_4 \frac{\varepsilon^2}{k} + c_5 \frac{\partial}{\partial z} \left(K_m \frac{\partial \varepsilon}{\partial z} \right), \quad (4.17)$$

where c_3, c_4 and c_5 are constants. The development of this popular scheme (according to Pope 2000) is credited to Jones and Launder (1972).

The $k - \varepsilon$ closure is a popular model, however it has often been found to produce excessively deep boundary layers which may be due to the imbalance between TKE production and dissipation. To resolve this issue a well known solution by Apsley and Castro (1997) limits the mixing length scale to either a finite ABL depth or the Obukhov length, depending on atmospheric stability. Conversely, Xu and Taylor (1997) suggest incorporating an additional production term into the TKE dissipation equation.

4.3.3 $k - l$ model closure

The $k - l$ scheme, also known as the $q^2 - l$ closure is originally derived from a simplified second order closure scheme (Mellor and Yamada, 1974). This scheme solves the prognostic equation for TKE as well as the prognostic equation for kl or l , where l is a “master turbulent length scale” (Weng and Taylor, 2003). Eddy diffusivity is calculated as

$$K = lqS_m \quad (4.18)$$

as given by Yamada (1983), where S_m is a stability function based on the flux Richardson number and $q^2 = 2k$

4.3.4 $\sigma_w^2 - \tau_w$ model closure

As discussed by Durbin (1991), the popular $k - \epsilon$ model specifically fails to adequately represent eddy viscosity very near boundaries (i.e., within the surface layer). In order to correct for these issues, Durbin suggests adopting a velocity scale which is the square root of the variance of vertical velocity $\sqrt{\sigma_w^2}$ (the standard deviation) such that

$$K = \sigma_w^2 \tau_w, \quad (4.19)$$

where τ_w is a turbulent time scale. As argued by Wilson (2012), Durbin's suggested velocity scale is a more generally appropriate choice (over any TKE parameterization), since (as proven by Taylor 1921) the velocity and length scales that define the eddy viscosity/diffusivity are statistics of *vertical* motion, and the TKE equation (which is incorporated within many eddy viscosity closure schemes) is dominated by statistics of *horizontal* motion (as illustrated in Equation 1.1). Also, the proposed method is rational, given the situation where there is no vertical velocity (i.e., $\sqrt{\sigma_w^2} = 0$), there will be no vertical transport of momentum via turbulent eddies. However, this scheme is not widely used and as such requires vigorous testing, although it has provided satisfactory results (Wilson, 2012) when compared to day 33 of the Wangara Boundary Layer Experiment (Clarke et al., 1971; Hess et al., 1981). It is the rationality of the proposed scheme that motivated this Master's Thesis project: testing the $K = \sigma_w^2 - \tau_w$ scheme against observations, the Bélair closure (Bélair et al., 1999) and the results discussed and examined in the second GABLS experiment (Svensson et al., 2011).

4.4 Second- and higher-order closures

As discussed in Section 3, equations to solve the covariances may be developed (whereas the covariances themselves are parameterized in first- and one-and-a-half-order schemes), which introduces third order moments (see Equation 3.4 as an example). It had been thought that by introducing higher order closures one was incorporating more of the physics involved, and thus, one would obtain more accurate results. These methods (second-order closure specifically) introduce covariances for pressure, transport terms of the third-order and dissipation terms (Garraff, 1992; Stull, 1988) which must be parameterized. Second-order closure also requires solving the equations from the one-and-a-half-order closures as well as equations for the second-order moments resulting in 6 equations with 10 unknowns for momentum only (see Stull 1988, Tables 6-1 and 6-2), which is much more computationally expensive than first- or one-and-a-half-order closures that requires solving respectively 3 and 6 equations and unknowns (as discussed in Section 3). Furthermore, third-order closure requires 10 equations and 15 unknowns. One must also consider equations for heat and humidity, as well as TKE, variances, covariances and other required parameters which again increases the number of equations needing to be solved. Therefore, lower order closure schemes are often more desirable.

4.5 Other models

Modeling the ABL is not limited to RANS approaches. Other methods such as Large Eddy Simulation (LES) are commonly used, but these methods are computationally expensive and significantly more complex than RANS methods alone. The principle behind LES is to model only the largest scales, i.e., the largest, high energy eddies, which have the greatest effect on the flow field and to parameterize the smallest scales, i.e., the smallest, low energy eddies, that have a lesser effect. The calculation of the flow field via LES requires several steps beyond the RANS (Ghosal and Moin, 1995). Initially, a filter is applied to the Navier-Stokes (and other governing) equations to remove small scales and retain only the large eddy scales. The size of scales removed may be dependent on distance from the surface as smaller turbulent scales

become increasingly important as distance from the surface decreases. The small scales which were removed are incorporated into an additional term which takes into account the effects of small scales on the larger turbulent motions through a stress tensor. This sub-grid scale stress tensor must be parameterized as the governing equations are unclosed. There are various methods to model these stress tensors, however, they will not be discussed here as the focus is on the RANS approach and *K*-Theory.

5 Methodology

The purpose of this research is to test and evaluate the $\sigma_w^2 \tau_w$ scheme as proposed by Wilson (2012) using a strict test specified by Svensson et al. (2011) for the second GABLS experiment. The second GABLS experiment (Svensson et al., 2011) examines the performance of a variety of eddy viscosity closure schemes (first-order and TKE based schemes) over an interval of several days over land. Participating models are forced by a specified time series in surface temperature, and all radiation schemes must be disabled.⁷ These restrictive conditions ensured all closure schemes were tested in a consistent manner such that the differences in model results are due mainly to differences in closure schemes. This experiment provided an excellent opportunity to test the performance of the alternative scheme which is the focus of the research presented here.

5.1 Model inter-comparison study: the second GABLS experiment and its specifications

The second GABLS experiment (Svensson et al., 2011) was chosen as a test for the alternative scheme presented in this thesis research since it is an easily implementable test which can be used to evaluate the performance of weather and climate models. It was the second in a series of studies which aim to improve model representation of the ABL. The first GABLS experiment (Cuxart et al., 2006) examined the performance of SCMs over land during weak stratification (in an idealized study); whereas the second GABLS experiment evaluated model performance over a full diurnal cycle using observations taken from the CASES-99 experiment (Poulos et al., 2002). The CASES-99 experiment was conducted during the entire month of October in 1999, and two clear consecutive dry days with a strong diurnal cycle were chosen for the second GABLS study. These days were chosen since the synoptic conditions were relatively unchanging and horizontally homogeneous, although only one of the two days selected illustrates nearly stationary conditions. Simple initial and boundary conditions were developed using data pro-

⁷Other specifications or prescriptions for the test are covered below.

vided from the CASES-99 experiment so that many groups were able to participate in the study since complicated processes (such as radiation schemes) would not influence model analysis and comparison. The remainder of this section and subsection outlines the $\sigma_w^2 - \tau_w$ model set-up based on conditions provided by Svensson et al. (2011).

The alternative model was run for a 59 hour simulation with a 60 s time step and was initialized at 1600 LT on October 22 for the location 37.6°N and 96.7°E . To align our study with the second GABLS experiment instructions, specific model parameters were adopted via specifications found in the Svensson et al. (2011) Appendix. The model domain is 4000 m deep, the lowest grid point is below 1 m, the grid contains 100 grid points, and the resolution is finer than 100 m for the entire domain. Roughness length is $z_0 = 0.03$ m and thermal roughness is $z_{0T} = 0.003$ m. Reference temperature and pressure are $\theta_0 = 283.15$ K and $p_0 = 1000$ hPa and the gravitational constant is $g = 9.81\text{ms}^{-2}$. Geostrophic wind remains constant for the entire simulation where $u_g = 3\text{ms}^{-1}$ and $v_g = -9\text{ms}^{-1}$. Initial vertical velocities are $w = 0$, until 1600 LT on October 23, when large scale divergence is introduced as

$$w = \begin{cases} -0.005 \frac{z}{1000} \text{ ms}^{-1} & \text{if } z < 1000 \text{ m} \\ -0.005 \text{ ms}^{-1} & \text{if } z \geq 1000 \text{ m.} \end{cases} \quad (5.1)$$

Boundary and initial conditions were also provided and further discussion can be found in subsection 5.2.5.

After the code was debugged and tested, the model was compared to observations taken on October 22, 1999 in Kansas during the CASES-99 study, (Poulos et al., 2002)⁸. The quantities compared include: the surface heat flux, 2 m temperature, 10 m wind speed, the surface friction velocity, the stability dependent drag coefficient, TKE, vertical velocity variance and the Obukhov length. Profiles for temperature, wind speed and TKE are also compared for October 23, at 14:00 local time.

⁸Data is available for download at <http://www.eol.ucar.edu/projects/cases99/>

5.2 The $\sigma_w^2 - \tau_w$ model

The time and height dependent single column model developed and written by Wilson (2012) solves the mean momentum equations for zonal and meridional wind speeds, and the equations for temperature and humidity in a horizontally homogeneous atmosphere using an eddy viscosity closure. It is written in the programming language Fortran-90 and the execution time to run a 59 hour simulation (as required by the second GABLS experiment) with 100 grid points and a 60 second time step (using a 64-bit operating system with 4 GB of RAM and an Intel(R) Core(TM) i7 860 @ 2.8 Ghz processor) is approximately four minutes. The model incorporates a finite volume method whereby the differential equations are integrated over a control layer prior to their discretization, and an optional Crank-Nicholson method can be used to integrate forward in time⁹. This results in a tridiagonal matrix of coefficients, $[M]$, such that the column vector for (as an example) the zonal velocity, $[u]$, at a set of n levels is given by $[M][u] = [B]$ where the coefficient matrix $[M]$ is $n \times n$. Then $[u] = [M]^{-1}[B]$ and as $[M]$ is tridiagonal, the solution $[u]$ is obtained using a tridiagonal matrix algorithm (TDMA) with a relaxation incorporated for all solved values to ensure convergence of the solutions.

5.2.1 Model equations

The equations solved (under the eddy viscosity closure assumption and henceforth dropping the over-bars) include:

$$\frac{\partial u}{\partial t} = \frac{\partial}{\partial z} \left[K \frac{\partial u}{\partial z} \right] - \frac{\partial uw}{\partial z} + f(v - v_g), \quad (5.2)$$

and

$$\frac{\partial v}{\partial t} = \frac{\partial}{\partial z} \left[K \frac{\partial v}{\partial z} \right] - \frac{\partial vw}{\partial z} - f(u - u_g), \quad (5.3)$$

⁹The model results presented within this thesis were solved using a fully implicit scheme.

$$\frac{\partial k}{\partial t} = K \left[\left(\frac{\partial u}{\partial z} \right)^2 + \left(\frac{\partial v}{\partial z} \right)^2 \right] - \frac{g}{\theta_0} K \frac{\partial \theta}{\partial z} - \frac{c_k k^{\frac{3}{2}}}{l_w} + \frac{\partial}{\partial z} \left[K \frac{\partial k}{\partial z} \right] - \frac{\partial k w}{\partial z}, \quad (5.4)$$

$$\frac{\partial \sigma_w^2}{\partial t} = -2 \frac{g}{\theta_0} K \frac{\partial \theta}{\partial z} - c_2 \frac{\sigma_w^2}{\tau_w} + c_1 \frac{\frac{2}{3} k - \sigma_w^2}{\tau_w} + \frac{\partial}{\partial z} \left[K \frac{\partial \sigma_w^2}{\partial z} \right] - \frac{\partial \sigma_w^2 w}{\partial z}, \quad (5.5)$$

$$\frac{\partial \theta}{\partial t} = \frac{\partial}{\partial z} \left[K \frac{\partial \theta}{\partial z} \right] - \frac{\partial \theta w}{\partial z}, \quad (5.6)$$

and

$$\frac{\partial Q}{\partial t} = \frac{\partial}{\partial z} \left[K \frac{\partial Q}{\partial z} \right] - \frac{\partial Q w}{\partial z}. \quad (5.7)$$

Equations 5.2 to 5.7 optionally include subsidence through the $-\frac{\partial a w}{\partial z}$ term, where a is a generic mean variable. In these equations t is time; z is the height above ground; K is the eddy diffusivity (or viscosity) solved using Wilson's (2012) eddy viscosity closure; u , v and w are the zonal, meridional and vertical wind speeds; u_g and v_g are the zonal and meridional geostrophic wind speeds (and can be thought of as parameterizing the large scale pressure gradient shown in the earlier equations); k is TKE; c_k , c_1 and c_2 are constants; σ_w^2 is the variance of the vertical velocity; g is the gravitational constant; θ is potential temperature; Q is specific humidity and l_w is the length scale implied by Wilson's (2012) formulation of K , i.e.,

$$l_w = \frac{\sigma_w^2 \tau_w}{(c_k k)^{\frac{1}{2}}}. \quad (5.8)$$

It is important to note, that the turbulent Schmidt and Prandtl number are assumed to be 1 for all model runs in this project and are thus not included in the given equations. This is not a universally valid assumption and the model does allow these numbers to vary from 1, but for the sake of simplicity they were omitted from the equations shown above.

As previously discussed, eddy viscosity is modeled using the first order closure scheme originally suggested by Durbin (1991), where

$$K = \sigma_w^2 \tau_w. \quad (5.9)$$

The turbulent time scale is determined (on no stronger basis than intuition and simplicity) as

$$\frac{1}{\tau_w} = \frac{1}{\tau_{w,SL}} + N + \frac{1}{\tau_\infty}, \quad (5.10)$$

where

$$\tau_{w,SL} = \frac{k_v u_* z}{\sigma_w^2 \phi_m \left(\frac{z}{L}\right)} \quad (5.11)$$

is the surface layer time scale according to Monin-Obukhov Similarity Theory (MOST) and

$$N = \begin{cases} 0 & \text{if } \frac{\partial \theta}{\partial z} \leq 0 \\ \left(\frac{g}{\theta_0} \frac{\partial \theta}{\partial z}\right)^{\frac{1}{2}} & \text{if } \frac{\partial \theta}{\partial z} > 0 \end{cases} \quad (5.12)$$

is the buoyancy frequency. τ_∞ is effectively the limiting time scale for unstable or neutral conditions in the outer layer. The dimensionless function $\phi_m \left(\frac{z}{L}\right)$ is calculated as

$$\phi_m = \begin{cases} \left(1 - 28 \frac{z}{L}\right)^{\frac{1}{4}} & \text{if } L < 0 \\ \left(1 + 5 \frac{z}{L}\right) & \text{if } L \geq 0 \end{cases} \quad (5.13)$$

(Dyer and Bradley, 1982).

After several model runs it became obvious that damping of the eddy viscosity was needed in order to smooth out oscillations in the output (see Figure 5.1). This was achieved by slowly introducing the newly calculated value of eddy viscosity into the model over each iteration until the solution has converged, i.e.,

$$K_p = r K_p^0 + (1 - r) K_p, \quad (5.14)$$

where K_p is eddy viscosity at a given grid point for the current time step, K_p^0 is eddy viscosity at

the given grid point at the previous time step, and r is the relaxation coefficient taken to be 0.96. Relaxation is imposed upon wind speed, temperature and humidity in the same way.

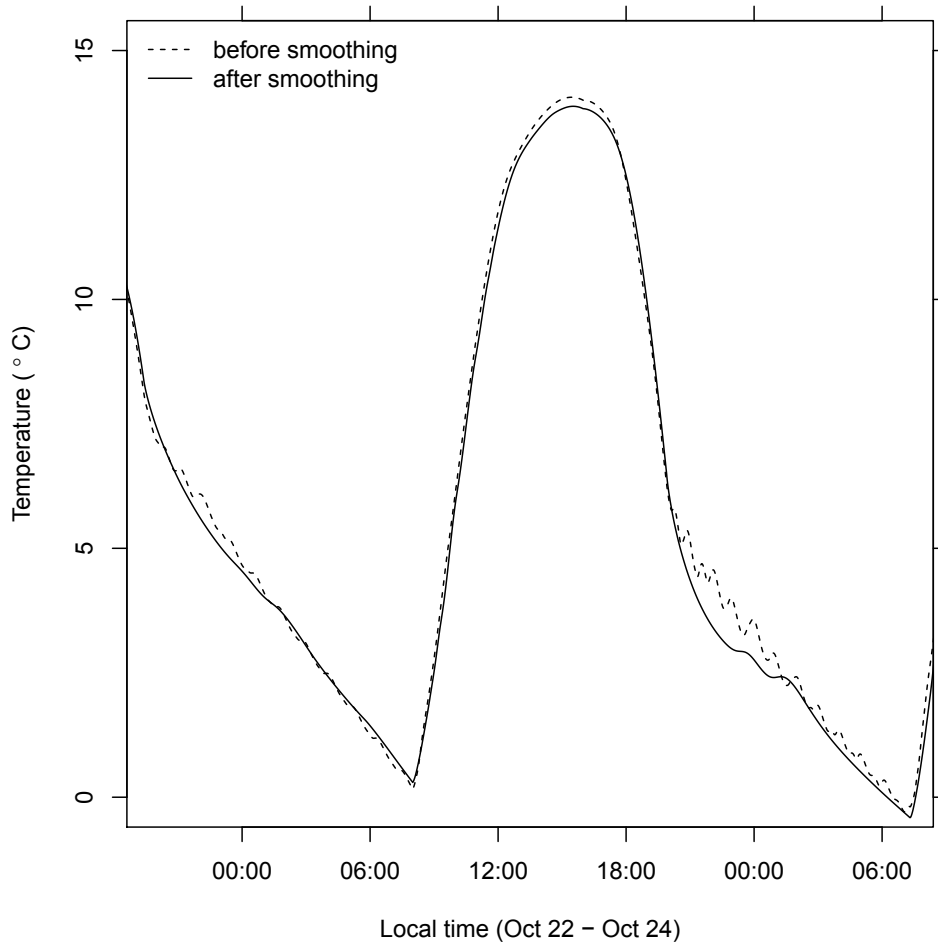


Figure 5.1: Time series of temperature at 2 m AGL. The solid black line is model output after incorporating a relaxation on eddy viscosity and the dashed line is before relaxation is applied

When running the Bélair scheme for the same experiment, there were no oscillations, so it appears the needed smoothing is the result of stability issues within the $\sigma_w^2 - \tau_w$ scheme only.

5.2.2 The surface layer within the model

As described in Section 2.1, the surface layer can be modeled using Monin-Obukhov similarity theory. This is an excellent theory and is used to couple the lowest grid point to the surface within the model. Similarly, MO time scales are incorporated into model equations; however, the model does not distinguish a surface layer in which the MOST is applied since the model,

by design, produces MO-like profiles near the surface. See Appendix A.

5.2.3 Discretization

As previously discussed, the model is built using a finite volume method, whereby the differential equations are integrated over a control layer prior to their discretization and a Crank-Nicholson method is optionally available to integrate forward in time. As an example, the zonal momentum equation (Equation 5.2) is integrated,

$$\int_s^n \int_t^{t+\Delta t} \frac{\partial u}{\partial t} dt dz = \int_s^n \int_t^{t+\Delta t} \left\{ \frac{\partial}{\partial z} \left[K \frac{\partial u}{\partial z} \right] - \frac{\partial u w}{\partial z} + f(v - v_g) \right\} dt dz, \quad (5.15)$$

where the limits of integration n and s indicate the top and bottom of the control layer over which the equation is being integrated (see Figure 5.2 as a simple example). It should be noted that the model tested here can optionally incorporate a uniformly spaced grid, however, it is tested using a log linear grid which is discussed in further detail below.

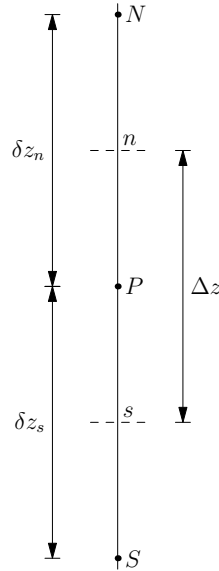


Figure 5.2: Uniformly spaced grid control layer for illustrative purposes. N , P and S indicate grid points, and n and s are the upper and lower limits of the control layer

The integration (without incorporating a Crank-Nicholson scheme for the sake of simplicity)

results in a fully implicit discretized equation,

$$(u_P - u_P^0) \frac{\Delta z}{\Delta t} = K_n \frac{u_N - u_P}{\delta z_n} - K_s \frac{u_P - u_S}{\delta z_s} - (u_n w_n - u_s w_s) + f(v_P - v_{gP}) \Delta z, \quad (5.16)$$

where the subscripts n , s , P , N and S indicate the variable is taken at the grid point corresponding to Figure 5.2. Equation 5.16 is subsequently rearranged, gathering similar terms, so that the tridiagonal matrix of unknown coefficients can be assembled and the new solution is found at each time step by way of the TDMA as was previously discussed.

5.2.4 Grid

The model grid point located closest to the ground is at the roughness height z_0 (which is related to the physical roughness of the surface) where the lowermost values TKE and vertical velocity variance are stored, and the uppermost values of wind speed, temperature and specific humidity are stored at the highest grid point. The grid is staggered such that levels where TKE and vertical velocity variance values are stored alternate with levels where wind speeds, temperature, and humidity values are stored. Using Figure 5.2 as an example, wind speed, temperature and humidity would be stored at levels S , P , and N and TKE and vertical velocity variance would be stored at levels s and n within the diagram (or vice versa).

The grid is specified such that the grid points follow a log linear profile. The purpose for the log linear profile is twofold. First, Svensson et al. (2011) suggest (but do not require) a log linear grid, and second, it is desirable to have a finer grid closer to the surface so that the model can resolve smaller turbulent features, since the length scales associated with turbulent motions decrease towards the surface. This profile is determined by integrating the reciprocal of a neutral length scale over the model domain and equating it to the integral of the reciprocal reference length scale for the transformed grid, as follows:

$$\frac{dz}{dz_*} = \frac{k_v z}{l_* (1 + \beta z/z_t)} \quad (5.17)$$

is integrated

$$\int_{z_0}^z \left[\frac{1}{k_v z} + \frac{\beta}{k_v z_t} \right] dz = \int_0^{z_*} \frac{1}{l_*} dz_* \quad (5.18)$$

so that we find

$$\frac{1}{k_v} \left[\ln \left(\frac{z}{z_0} \right) + \beta \frac{z - z_0}{z_t} \right] = \frac{z_*}{l_*}. \quad (5.19)$$

In the above equations

$$\beta = \frac{k_v z_t}{l_\infty}, \quad (5.20)$$

$$l_\infty = \sqrt{u_g^2 + v_g^2} \frac{0.0004}{f} \quad (5.21)$$

as used by Delage (1974), and

$$l_* = \frac{k_v z_t}{\ln \frac{z_t}{z_0} + \beta \left(1 - \frac{z_0}{z_t} \right)}. \quad (5.22)$$

Furthermore, within these equations, z is the height of the model grid point, z_t denotes the depth of the model domain, z_* represents the transformed coordinate¹⁰ corresponding to the log linear model grid point, l_* is the reference length scale (which was found by integrating Equation 5.18 over the entire domain), l_∞ is the limiting length scale calculated according to Delage (1974) and β denotes a Blackadar constant. As the solution cannot be directly calculated for height of the grid points from Equation 5.19, a Newton-Raphson iterative method is implemented. The location of selected grid points is shown in Table 5.1 for a grid with 100 grid points and a domain of 4000 m (the grid used for this thesis research).

¹⁰Which is determined by equally spacing points that are separated by the total domain height divided by the number of grid points; e.g., the 4th grid point from the bottom, if the grid was 1000 m and contained 101 grid points, would be located at 30 m.

Grid point	Height above ground (m)
100	4000
50	1476
20	145.3
10	3.97
9	2.46
8	1.52
7	0.93
6	0.57
5	0.35
4	0.21
3	0.13
2	0.08
1	0.05

Table 5.1: Model grid point height examples where wind speed, temperature and humidity are calculated. Grid points for TKE and vertical velocity variance are located half way between the wind speed, temperature and humidity grid points

5.2.5 Initial and boundary conditions

The initial conditions are provided for potential temperature and humidity profiles based on instructions given by Svensson et al. (2011) as seen in Table 5.2. All temperature and humidity values between the given values are linearly interpolated. The initial TKE profile¹¹ is specified as

$$k = \begin{cases} 0.5 \left(1 - \frac{z}{800}\right) & z \leq 800 \\ 0 & z > 800 \end{cases} \quad (5.23)$$

General power-law wind profiles,

¹¹The TKE profile was not provided by Svensson et al. (2011), but was provided to the participating modelers through instructions found at http://people.su.se/~gsven/gabls/Case_description_Gabls2.pdf.

$$u_j = u_g \left[\frac{z_j}{z_{j_{max}}} \right]^{\frac{1}{7}} \quad (5.24)$$

and

$$v_j = v_g \left[\frac{z_j}{z_{j_{max}}} \right]^{\frac{1}{7}}, \quad (5.25)$$

are implemented initially for zonal and meridional wind speed as no initial profile for wind speed is given and the model is given sufficient spin up time, i.e., the model runs for a minimum of 5 hours (before examining model results) to ensure that any initial conditions would be “forgotten” and the model would be driven (influenced) only by the prescribed forcing, i.e., known constant geostrophic wind and evolving surface temperature. In these equations the subscript j is the grid point index with j_{max} referring to the uppermost grid point. As σ_w^2 is not specified, the initial value of 0.1 is assigned over the entire domain and the model is allowed to evolve to steady state, holding u, v, θ and Q constant, subsequently providing an initial profile. Finally, initial surface pressure is 972 hPa.

θ (K)	Q (kg kg ⁻¹)	z (m)
312	0.0015	4000
310	0.0020	3500
300	0.0030	2000
292	0.0005	1000
288	0.0025	900
286	0.0025	850
286	0.0025	200
288	0.0025	0

Table 5.2: Initial conditions for potential temperature and specific humidity as specified by Svensson et al. (2011)

As the lowest grid points for k and σ_w^2 are located at the ground (z_0), the boundary conditions are specified as

$$k = \frac{\phi_{uu} + \phi_{vv} + \phi_{ww}}{2} u_*^2 \quad (5.26)$$

and

$$\sigma_w^2 = \phi_{ww} u_*^2 \quad (5.27)$$

where ϕ_{uu} , ϕ_{vv} and ϕ_{ww} are universal velocity variance functions given by MOST and are assigned, within the model, their equilibrium values (for $z/L=0$) of 2.0, 2.0 and 1.3 respectively. Grid points for u , v , θ and Q are, however, located above the surface and flux boundary conditions at ground level are needed. The surface fluxes of heat and vapor are calculated:

$$\overline{w'\theta'_0} = -u_*\theta_*, \quad (5.28)$$

and

$$\overline{w'Q'_0} = -0.025u_*Q_{*pot}, \quad (5.29)$$

where $\overline{w'\theta'_0}$ is the surface heat flux, $\overline{w'Q'_0}$ is the surface humidity flux (which is calculated, according to the prescription of the model test, as 2.5% its potential value). The scales required for the surface fluxes are calculated as

$$\theta_* = k_v \frac{\theta_1 - \theta_{skin}(t)}{\ln\left(\frac{z_1}{z_{0T}}\right)}, \quad (5.30)$$

which is a temperature scale and

$$Q_{*pot} = k_v \frac{Q_1 - Q_{sat}(\theta_{skin}, p)}{\ln\left(\frac{z_1}{z_{0T}}\right)}, \quad (5.31)$$

which is a humidity scale calculated based on saturation at the surface. In these formulas θ_1 , Q_1 and z_1 indicate the potential temperature, specific humidity and height at the lowest grid point,

$\theta_{skin}(t)$ is the prescribed surface temperature (which is a function of time), Q_{sat} is the surface specific humidity at saturation (for current temperature and pressure) and z_{0T} is the roughness length for temperature and humidity.

The friction velocity was determined as

$$u_* = \sqrt{C_D (u_1^2 + v_1^2)} \quad (5.32)$$

where

$$C_D = \left[\frac{k_v}{\ln\left(\frac{z_1}{z_0}\right)} \right]^2 \quad (5.33)$$

is the neutral drag coefficient and u_1 and v_1 are respectively zonal and meridional velocities at the lowest grid point¹². Surface drag, S , is incorporated into the zonal and meridional velocity equations, at the lowest grid point, such that it acts in the opposite direction of the wind. For further derivations see Appendix B.

The model is driven by prescribed skin temperature (see Table 5.3) as given in the Svensson et al. (2011) Appendix; however, for the purposes of this research, the time series is shifted ahead two hours (from the time series provided in the Svensson et al. (2011) Appendix) to better match the data. When initially plotting the driving surface temperature, it was obvious that there was a two hour discrepancy between the time series 2 m temperature as plotted by Svensson et al. (2011) and the driving surface temperatures as given in the article's Appendix. This discrepancy was also found when comparing the driving surface temperatures to the raw data obtained from the CASES-99 experiment. Clarification was requested from the corresponding author for the two hour time discrepancy through an e-mail directly to the provided e-mail address, but the corresponding author did not reply. It was confirmed that local sunrise (and hence surface warming) is consistent with the temperature trends plotted in the second GABLS experiment and with the CASES-99 experiment data, so the driving surface temperature was shifted forward without the

¹²The lowest grid point is sufficiently close to the ground that no stability correction is required when deriving C_D ; the same approximation is inherent in Equations 5.30 and 5.31.

benefit of any consultation.

$T = -10 - 25 \cos(0.22(t - 2) + 0.2)$	$t - 2 \leq 17.4$
$T = -0.54(t - 2) + 15.2$	$17.4 < t - 2 \leq 30$
$T = -7 - 25 \cos(0.21(t - 2) + 1.8)$	$30 < t - 2 \leq 41.9$
$T = -0.37(t - 2) + 18.0$	$41.9 < t - 2 \leq 53.3$
$T = -4 - 25 \cos(0.22(t - 2) + 2.5)$	$53.3 < t - 2 \leq 65.6$
$T = 4.4$	$t - 2 > 65.6$

Table 5.3: Time series of surface temperature ($^{\circ}\text{C}$) (Svensson et al., 2011) adjusted 2 hours forward in time, where t is time in hours

The model prescribes temperature and humidity to be constant at the uppermost grid point which is determined to be the respective value at the highest grid point during initialization. TKE and vertical velocity variance are both prescribed as vanishing at the upper boundary. Upper boundary conditions for u and v are such that $u = u_g$ and $v = v_g$. At every time step, the model determines where TKE vanishes above the boundary layer and at all grid points above the ABL u and v are held at the constant geostrophic wind speed. This is required due to the effectively negligible eddy diffusivity and eddy viscosity above the (computed) ABL where stratification is extremely stable, with the consequence that the boundary conditions at the uppermost grid point are not properly coupled through the free atmosphere to the top of the ABL.

5.3 Tower data

High-rate observational data for the main 55 m tall tower was obtained from the University Corporation for Atmospheric Research (UCAR). The data archive and instrument information is available at <http://www.cora.nwra.com/cases/CASES-99.html>. The main tower was located at 37.64855°N and $-96.73610^{\circ}\text{W}$. Data was sampled at eight different heights between 1.5 m to 55 m where measurements were taken at 20 samples per second for wind speed, temperature, water vapor concentration and carbon dioxide concentration. Data provided by UCAR at each

height are given in Table 5.4.

height(m)	Variables
55	u, v, w, T_v, ρ_v
50	u, v, w, T_v
40	$u, v, w, T_v, \rho_v, r_c$
30	u, v, w, T_v
20	$u, v, w, T_v, \rho_v, r_c$
10	u, v, w, T_v
5	$u, v, w, T_v, \rho_v, r_c$
1.5	u, v, w, T_v

Table 5.4: Variables at given tower height for the CASES-99 experiment provided by UCAR (u, v and w are corrected for sonic tilt). u, v and w are the zonal, meridional and vertical wind speeds (ms^{-1}), T_v is virtual temperature ($^{\circ}\text{C}$), ρ_v is the water vapor density from a Campbell krypton hygrometer (g m^{-3}) and r_c is the CO_2 mixing ratio (mg m^{-3})

Low-rate data was also provided by UCAR (sampled every 5 seconds) for surface pressure which was used to convert temperature to potential temperature and water vapor density to specific humidity.

30 minute statistics (e.g., means, covariances etc.) were calculated for each variable in order to compute fluxes for momentum, heat and water vapor. The Schotanus (Schotanus et al., 1983) and WPL (Webb et al., 1980) corrections were applied to account for temperature and water vapor fluctuations (WPL) and the measurement of temperature using speed of sound by the sonic anemometer (Schotanus). For specific details on the corrections see Appendix C. As the tower data did not contain near ground measurements, nor did it contain measurements at all the required heights (e.g., 2 m temperatures), MOST was used to fit temperature, wind and humidity profiles to the data sampled in the surface layer (see Appendix D). These profiles were then used to estimate values at the specified heights where no observations were taken so that comparisons could be made between the model and measurements.

5.4 Sounding data

Sounding data was obtained from the CASES-99 Data Archive¹³ for the Leon sounding station which is located nearby the main tower.

¹³<http://www.cora.nwra.com/cases/CASES-99.html>

6 Results

As previously discussed the model was run for 60 hours and was driven by constant geostrophic wind speed, and the prescribed time series for surface temperature and large scale divergence. A closure scheme formulated according to Bélair et al. (1999) was also used to compute an alternative evolution of the ABL that could be compared with the $\sigma_w^2 - \tau_w$ scheme¹⁴. Overall, the modeled results presented here are consistent with general findings for models presented by Svensson et al. (2011). All the statistics from observations as well as plots for all data were constructed using R statistical language (R Development Core Team, 2007).

6.1 Time series

Temperatures for the models as well as observations at 2 m and surface forcing are found in Figure 6.1. Initially, temperatures are modeled well by both schemes, although the Bélair model illustrates temperatures approximately 1°C warmer than the $\sigma_w^2 - \tau_w$ model predicts. The sudden rise in observed temperatures during the first night (at approximately 03:00 LT) is a local phenomenon (as noted by Svensson et al. 2011) which is not incorporated in the surface forcing and thus the disturbance is not seen in modeled results. During morning warming, both closures model temperature well. Peak afternoon 2 m temperatures are consistent between the two models and observations, which is unsurprising since during the most unstable time of day the 2 m temperatures should be most strongly coupled to the imposed surface temperature. The large difference in surface and model temperature late morning and early afternoon is due to the strong near surface temperature gradient and the height difference between surface and the 2 m level. When afternoon cooling begins, modeled temperatures cool slightly slower than observed until after sunset the second night when the models continue to predict temperatures higher than those observed. This may be in part due to the prescribed surface forcing as described by Svensson

¹⁴The Bélair closure scheme was tested in the second GABLS experiment, however, it was tested using the Meteorological Service of Canada model (where model differences, owing to the lower resolution of that implementation, may be significant when compared to the model used here). The Bélair results presented here are generally qualitatively similar (except the sensible heat flux and all profiles) when compared to the Bélair results found in the second GABLS experiment. This will be discussed further.

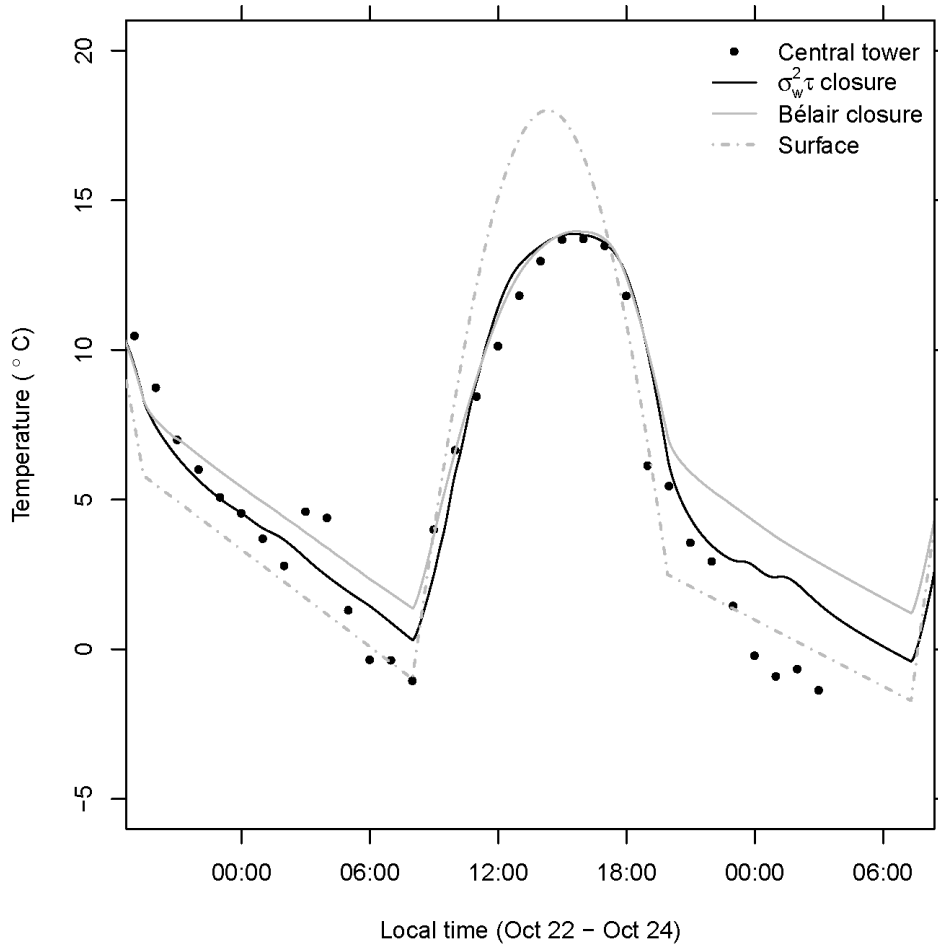


Figure 6.1: Time series of temperature at 2 m AGL. The black dots indicate Central Tower observations, the solid black line illustrates the $\sigma_w^2 - \tau_w$ model results, the solid gray line shows the Bélair closure results and the dashed-dotted gray line represents the prescribed skin temperature.

et al. (2011); the differences in observed surface temperature and surface forcing are noticeable after 18:00 LT (not shown). While both models are too warm the second evening, the $\sigma_w^2 - \tau_w$ closure 2 m temperatures are 1.5°C cooler than Bélair's. Both model temperatures fall within the range of temperatures produced by TKE based models in the second GABLS experiment.

Wind speed at 10 m is shown in Figure 6.2. During the first evening and morning the $\sigma_w^2 - \tau_w$ modeled wind speed matches observed wind speeds well, however, the Bélair closure generally over predicts wind speeds during this cooling phase. As morning heating commences there is a delay in the increase of modeled wind relative to observed wind, amounting to some 3-4 hours, something we are unable to explain. This occurs for both models and also occurs for many of

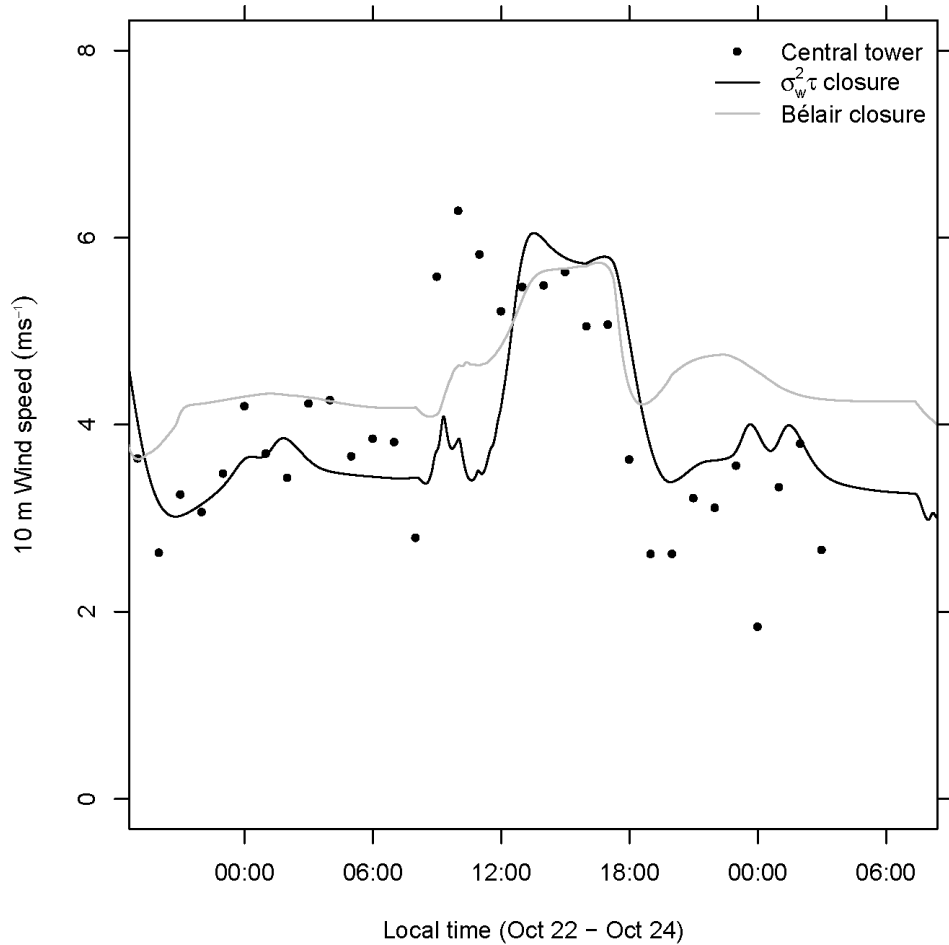


Figure 6.2: Time series of wind at 10 m AGL

the closure schemes presented in Svensson et al. (2011). The Bélair scheme illustrates gradually rising wind speeds, however, the $\sigma_w^2 - \tau_w$ shows a sudden increase in wind speed which drops off before increasing to the maximum wind speeds around noon. After noon, both models predict similar wind speeds which are consistent with those observed at 10 m until afternoon cooling. The $\sigma_w^2 - \tau_w$ turbulent decay and reduction of wind speed during the transition from unstable to stable conditions lags behind observations by approximately an hour.

A discrepancy between modeled and observed wind speeds the second evening is discussed by Svensson et al. (2011) as nearly all models in the second GABLS experiment overestimate the wind speed, which is likely due to imposed geostrophic winds that are too strong. This is consistent with findings here; late afternoon and evening of the second night modeled wind speeds are stronger than observed for the $\sigma_w^2 - \tau_w$ closure (the $\sigma_w^2 - \tau_w$ scheme wind speed during

this time is significantly closer to observations than the modeled wind for the Bélair scheme).

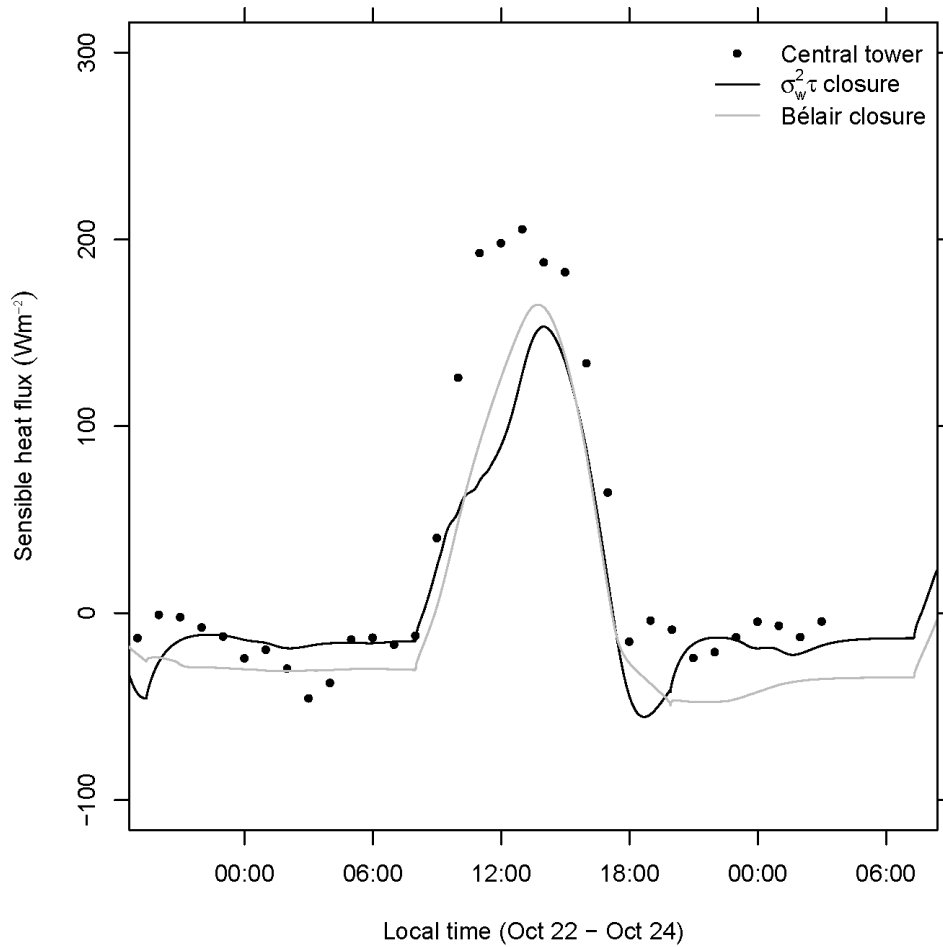


Figure 6.3: Time series of sensible heat flux

Figure 6.3 shows the sensible heat flux. Initially, $\sigma_w^2 - \tau_w$ shows a strong negative heat flux the first evening during the transition from day to night, which is also produced at the same time the next evening as expected. The local temperature increase during the first evening (around 03:00 LT) is visible within the observed sensible heat flux where the observations show a stronger downward flux than that which is modeled by both schemes; otherwise the sensible heat flux is modeled well by the $\sigma_w^2 - \tau_w$ scheme and modeled slightly too strong by Bélair's. During the transition from night to day (at approximately 08:00 LT), the sensible heat flux is modeled well, however late morning to early evening the modeled fluxes are consistently lower than observed for both models. The rate of increase is too slow during late morning; this coincides with the delay in increasing wind speeds as seen in Figure 6.2 which may be linked

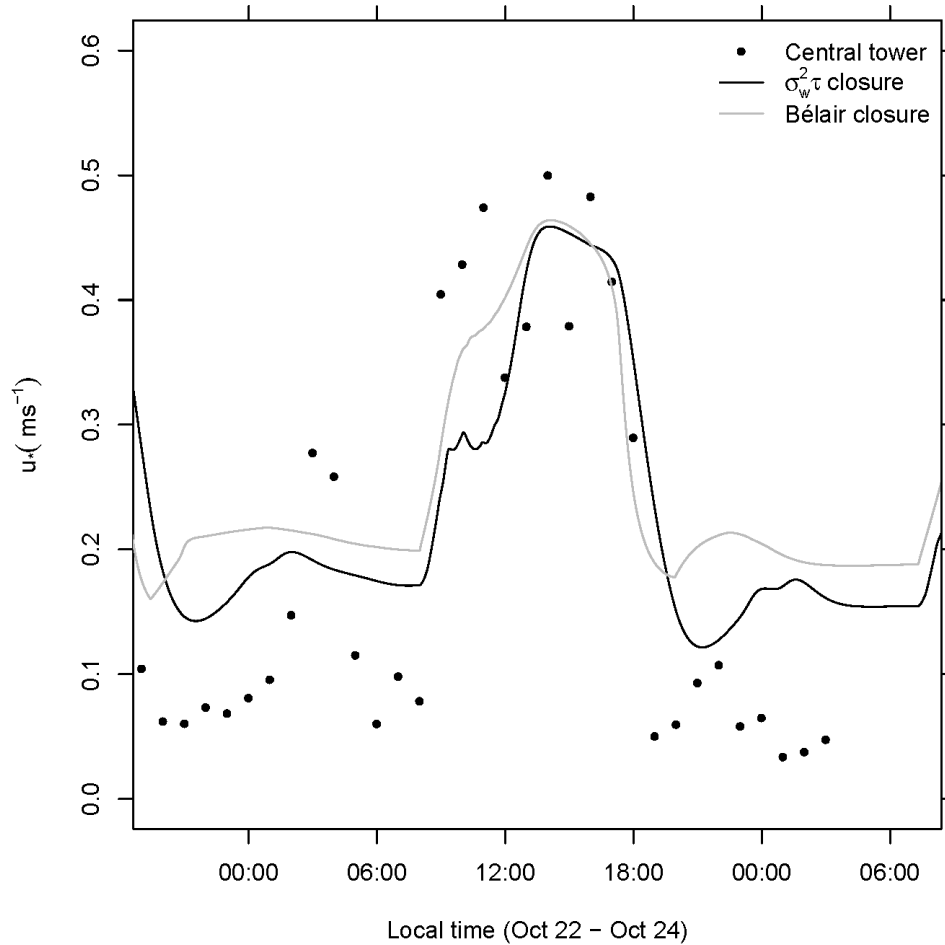


Figure 6.4: Time series of tower averaged friction velocity

to the incorrect rate of growth in the convective boundary layer. The maximum downward flux in the early evening of the second day is modeled at the correct time by the $\sigma_w^2 - \tau_w$ closure and according to the available observations, the heat flux is modeled well during the second night. The Bélair scheme illustrates a strong downward heat flux for the entire evening, which would be expected since its 2 m temperatures are modeled higher than those observed (see Figure 6.1). It should be noted that the Bélair scheme's sensible heat flux results published in the second GABLS experiment differ significantly from the results presented here, where the maximum sensible heat flux presented in the second GABLS experiment is approximately 110 Wm^{-2} and the maximum presented here is approximately 160 Wm^{-2} . This may be due to the use of different grids, and will be discussed further.

Figure 6.4 shows the friction velocity averaged over the height of the tower. This average

was obtained by determining the mean of all friction velocities computed at each measurement height. The tower averaged friction velocity was chosen to be presented as the observed turbulent momentum fluxes were erratic over the height of the tower whereas in principle a near constant value, or a systematic attenuation with increasing height, is expected. During the first night and morning both models predict friction velocities that are too high. Friction velocities in the second GABLS experiment during the evening and early morning are generally modeled too large as well by many of the models that were tested; thus the deviation between modeled results and observation is not likely due to a deficiency that is specific to the $\sigma_w^2 - \tau_w$ closure. The local temperature increase and its effects are also visible as an increase in measured friction velocity around 03:00 LT the first morning. Again, as expected, this disturbance is not modeled (see comments at the beginning of section 6 referring to Figure 6.1). During morning heating, both models show increases in friction velocity due to surface heating and turbulence at the correct time, although the $\sigma_w^2 - \tau_w$ model increases and remains nearly constant for two to three hours mid morning before increasing to a maximum in the afternoon. This is again coincident with the above observations for the lower rate of increase in the sensible heat flux and the delay in increases of wind speed. The Bélair scheme, while showing slightly slow rates of increase late morning, performed better. Both models show decreases in friction velocity at the correct time during late afternoon early evening cooling; however, like many models in the second GABLS experiment, both models predict friction velocities that are significantly higher than those observed during the second evening and night. Also, the $\sigma_w^2 - \tau_w$ model shows decreases in friction velocity at a slower rate than the observed and the Bélair scheme (similar to the $\sigma_w^2 - \tau_w$ results for 10 m wind speed).

The tower averaged drag coefficient is presented in Figure 6.5, which is computed as

$$C_D = \frac{u_*^2}{U_{10m}^2} \quad (6.1)$$

where C_D is the stability-dependent drag coefficient, u_* is the tower averaged friction velocity illustrated in Figure 6.4, and U_{10m} is the wind speed at 10 m, which is illustrated in Figure 6.2.

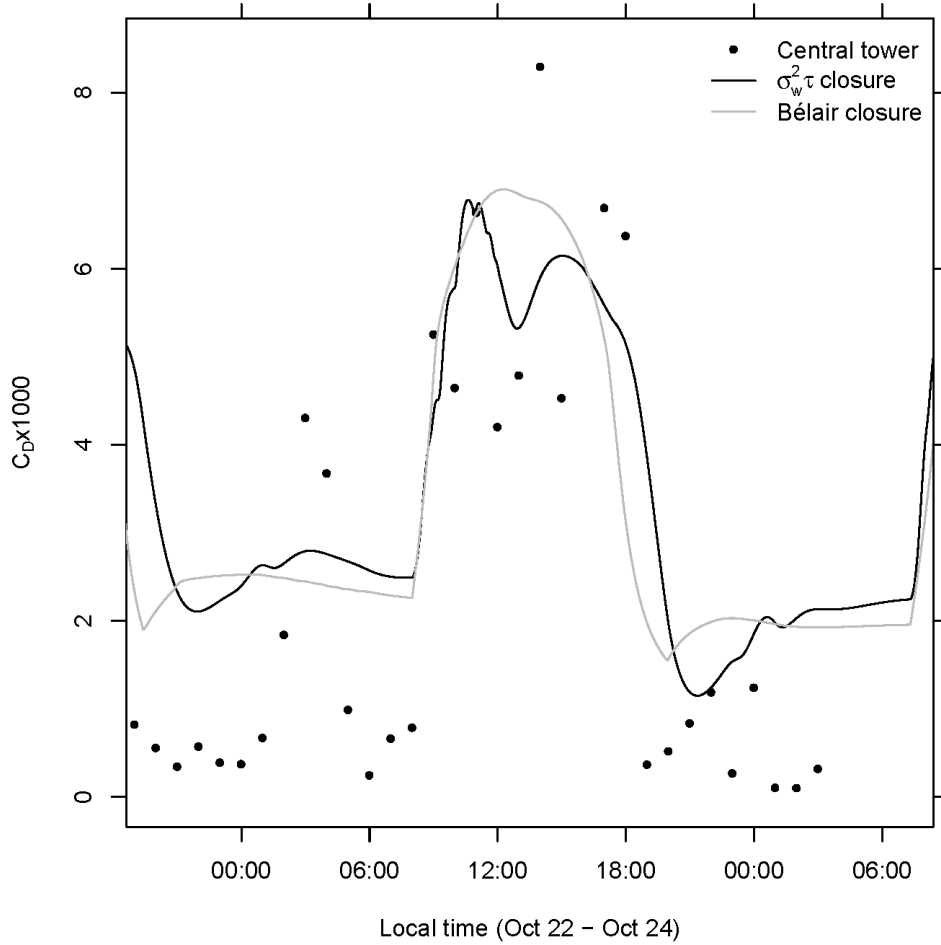


Figure 6.5: Time series of tower averaged stability-dependent drag coefficient

The results presented by Svensson et al. (2011) for the stable evening (not illustrated) show the drag coefficient modeled too large, while day time results are generally representative of the drag coefficient calculated from observed data. This is consistent with the results presented here; during the evening and early morning hours the drag coefficient is modeled too large by both models, and during the turbulent hours the drag coefficient is modeled well by both, except late during the late afternoon and early evening when turbulence begins to decay. Agreement in the drag coefficient during the late morning (but disagreement for friction velocity and wind speed) between the $\sigma_w^2 - \tau_w$ and Bélair schemes is explained by the low wind speeds modeled by the $\sigma_w^2 - \tau_w$ and Equation 6.1. As shown in the Kerang simulations in Appendix A, the proposed scheme models drag correctly. During the turbulent decay, the $\sigma_w^2 - \tau_w$ closure does not reduce drag quickly enough and lags behind the observations by approximately two hours which is

evident in the 10 m wind speed and friction velocities as well (Figures 6.2 and 6.4). A similar delay occurs for nearly all schemes presented in the second GABLS experiment.

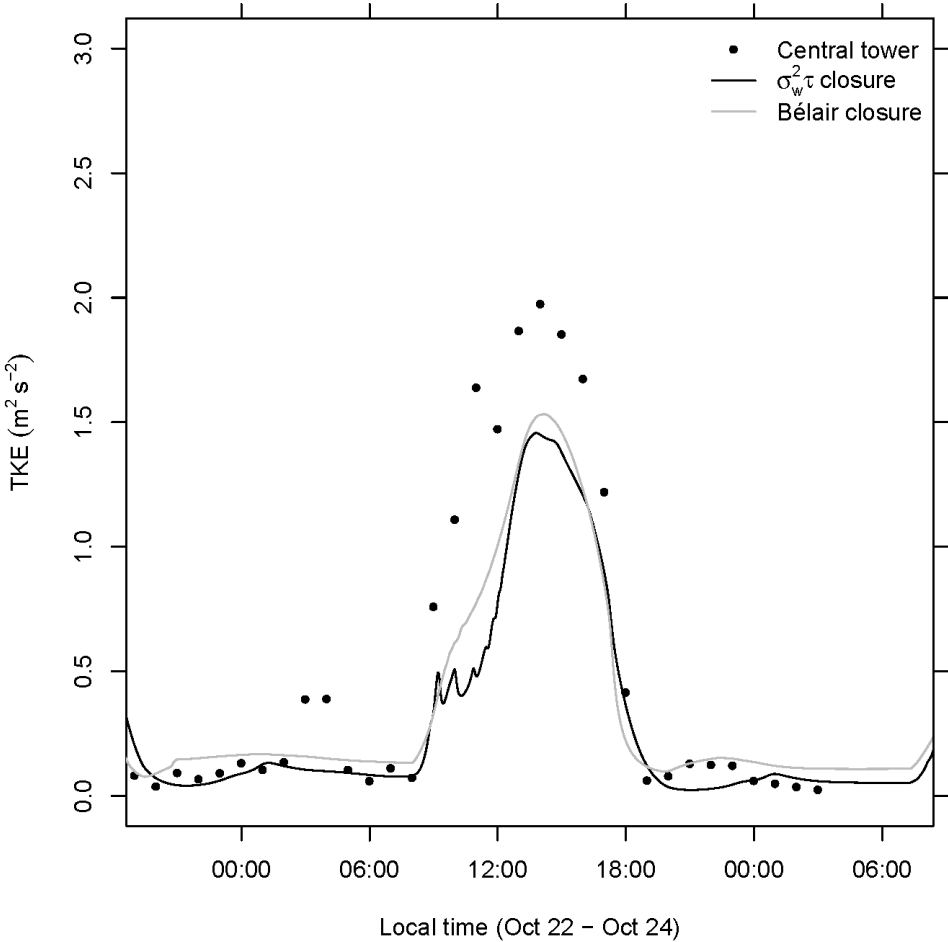


Figure 6.6: Time series of tower averaged turbulent kinetic energy

Figure 6.6 illustrates the tower averaged TKE. Again, as the turbulent fluxes were not consistent over height, it was necessary to average the fluxes in the same way as u_* ; TKE was also presented by Svensson et al. (2011) as a height averaged quantity. In general, Svensson et al. (2011) found that most models slightly over predict TKE during the night and under predict TKE during the day; again consistent with results presented here. TKE is modeled well in the evening and early morning for both days by the $\sigma_w^2 - \tau_w$ scheme and is modeled slightly high by the Bélair closure although it's maximum exceedance above the $\sigma_w^2 - \tau_w$ scheme is approximately $0.1\text{m}^2\text{s}^{-2}$ which occurs in the hours before midnight local time for both days. During

afternoon hours neither model produces enough TKE (a discrepancy of about 25%), and both models are approximately consistent in maxima and rates of change. The eddy diffusivity, being proportional to the square root of the TKE, could potentially result in approximately 10% of the error observed in the sensible heat flux (Figure 6.3).

As also seen in Figures 6.2, 6.3 and 6.4, Figure 6.6 illustrates a slow ramping up of TKE, suggesting that the models are not producing enough turbulence during the morning which results in less mixing and lower values for wind speeds, sensible heat flux, friction velocity and TKE during the onset of atmospheric instability.

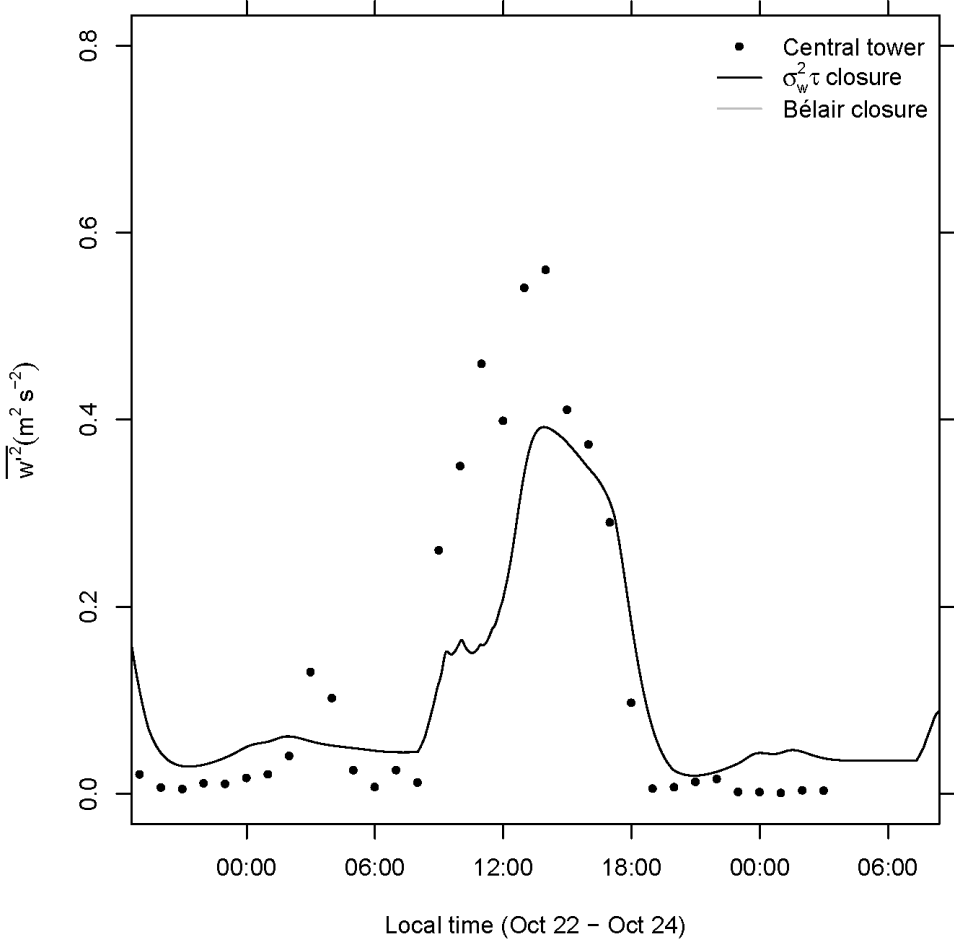


Figure 6.7: Time series of tower averaged vertical velocity variance

Vertical velocity variance averaged over the tower is presented in Figure 6.7. As the Bélair scheme does not require vertical velocity variance, and thus it is not calculated, the results for

the $\sigma_w^2 - \tau_w$ scheme are presented alone. The slow ramping up of turbulence is evident again in the morning hours during heating as observed in the figures previously discussed. During the evening the vertical velocity variance is modeled too high and during most of the daytime it is modeled too low, as is also the general result in the second GABLS experiment. Both the second GABLS experiment and the model results presented here show better agreement between modeled and observed vertical velocity variance in the late afternoon than in the late morning and early afternoon. During the afternoon cooling period, at approximately 18:00 LT, the rate of decrease in vertical velocity variance is consistent with the observations (although it appears to lag behind the observations by approximately an hour as seen in wind speed and friction velocity).

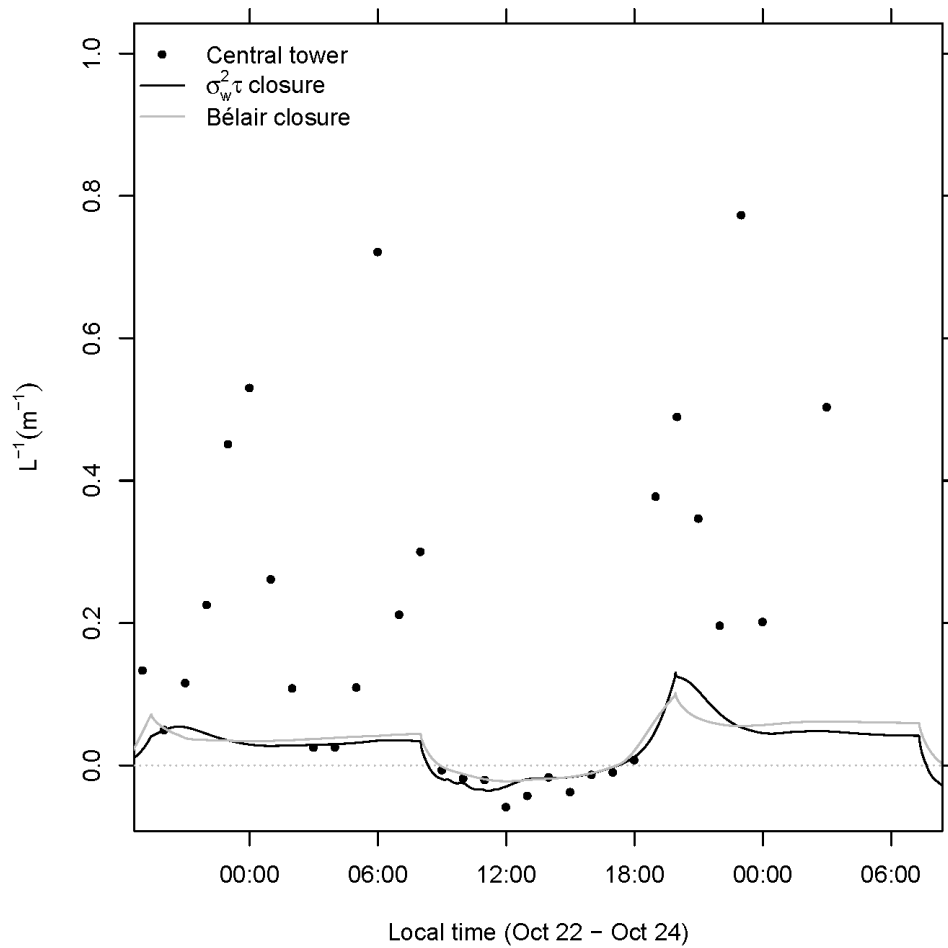


Figure 6.8: Time series of inverse Obukhov length

Unlike the results presented by Svensson et al. (2011) for the second GABLS experiment, we have chosen to present the inverse Obukhov length as seen in Figure 6.8. These results are also height averaged. As infinite values of L indicate neutral stratification, it is most convenient to present L^{-1} . During night and morning hours both models produce the correct stability class which is the same as those seen in the observations (i.e., the correct sign associated with stability or instability), although the observations show a significantly more stable atmosphere and a slightly more unstable atmosphere during the evening and day time respectively. These results appear to be consistent with the other models tested, according to unpublished results¹⁵, as all models shown produce roughly the same magnitudes for L^{-1} as the $\sigma_w^2 - \tau_w$ and Bélair schemes shown here. Both models transition from stable to unstable and vice versa at the appropriate time (although the $\sigma_w^2 - \tau_w$ closure transitions from stable to unstable slightly before the observations and the Bélair scheme), and the models are consistent in magnitude of L^{-1} except during the evening of the second night, where the $\sigma_w^2 - \tau_w$ scheme illustrates slightly more stable conditions at approximately 20:00 LT.

6.2 Vertical profiles

The profiles for potential temperature as well as soundings for October 23, 2014 at 14:00 LT are presented in Figure 6.9. Very close to the surface, the potential temperature is well represented in both models, as expected since the model is driven by the imposed surface temperature. However, both models produce results that are as much as a degree too warm in the well mixed ABL. Similar to results presented by Svensson et al. (2011), the height of the ABL is not well represented by the $\sigma_w^2 - \tau_w$ model (which may be the result of excess mixing); it is better represented by the Bélair scheme. However, the Bélair scheme does not produce a strong enough inversion above the ABL, nor does it show a clear discontinuity between the well mixed layer and the inversion aloft, whereas the $\sigma_w^2 - \tau_w$ closure does (albeit the inversion is too far aloft). The results produced here by the Bélair scheme are significantly different from those presented

¹⁵Results can be found at <http://people.su.se/~gsven/gabls/Results/index.html>.

in the second GABLS experiment, where the potential temperature in the well mixed region is as much as two degrees cooler. This is again likely the result of differing grids and it will be discussed further.

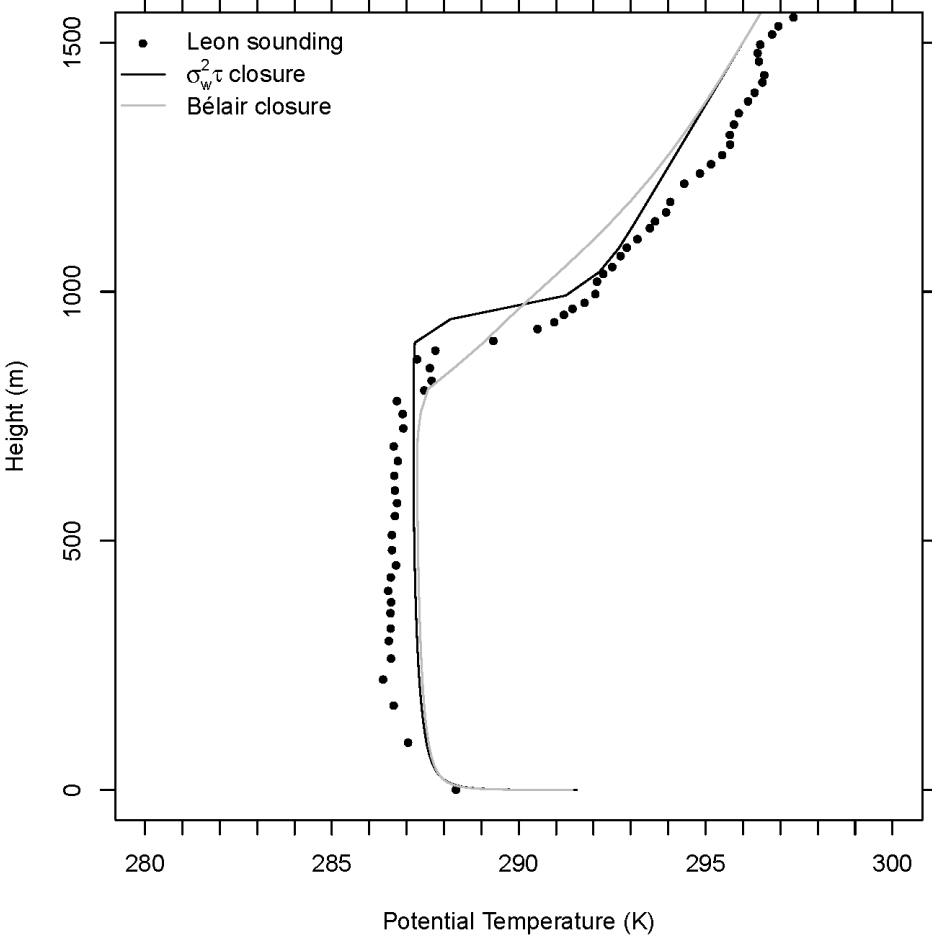


Figure 6.9: Potential temperature profiles for October 23, 14:00 LT; 22 hours after initialization

Generally both models produce satisfactory results for the wind profile on October 23, 14:00 LT which is seen in Figure 6.10, although it appears $\sigma_w^2 - \tau_w$ scheme produces slightly too much wind in the well mixed layer. Due to the erratic nature of the sounding data, it is hard to suggest which model’s performance is superior, although the height of the ABL is better predicted by the Bélair scheme as seen in the previous figure. As discussed by Svensson et al. (2011), other results from the CASES-99 experiment show almost constant wind speeds (from wind profilers and sodars) of approximately $5.5-6.5 \text{ ms}^{-1}$ in the mixed layer, which is lower than the model results as the Bélair closure and the $\sigma_w^2 - \tau_w$ scheme produce wind speeds of approximately 7

and 7.5 ms^{-1} respectively in the well mixed layer. In the second GABLS experiment, the models showed variable results for the wind speed profiles, although first order models with the finest grids produced the best results.

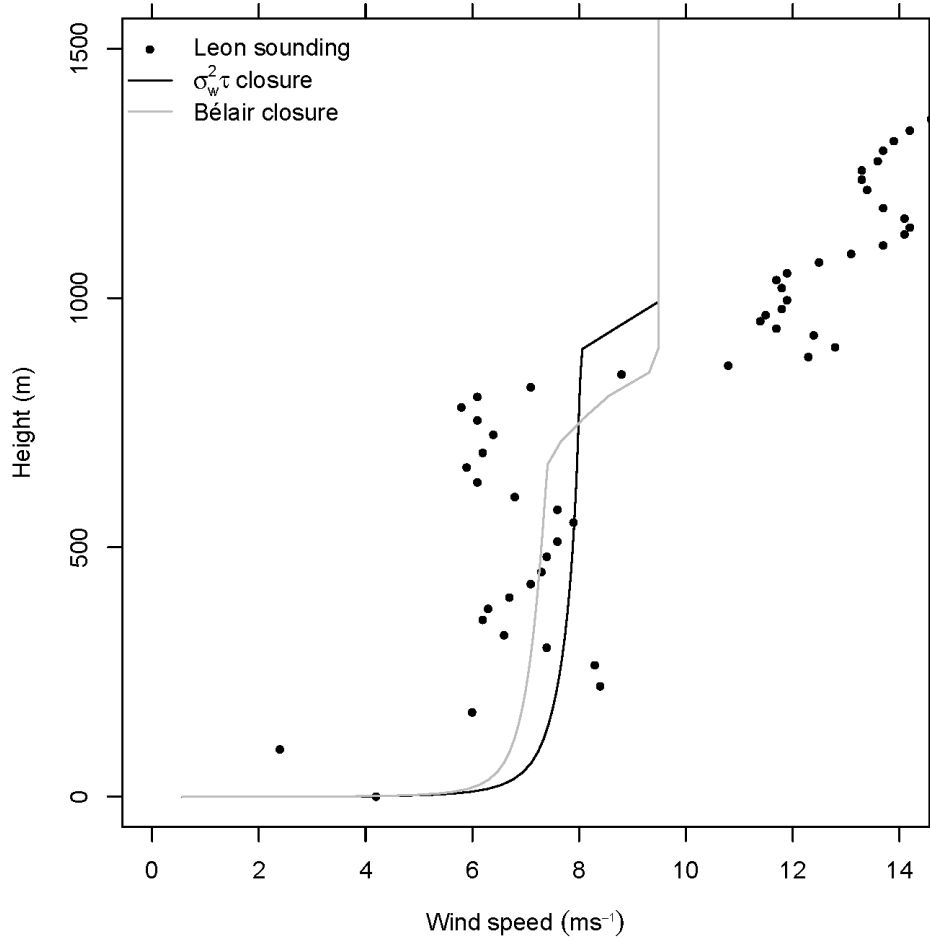


Figure 6.10: Wind speed profiles for October 23, 14:00 LT; 22 hours after initialization

The TKE profile is not available for the entire boundary layer, and as such only the model results are available for comparison in Figure 6.11. The models both produce comparable results for TKE in the lowest 750 m, although they diverge aloft clearly illustrating different ABL depths. These results fall within the range of results presented by Svensson et al. (2011), although the TKE results presented here are higher than the average TKE produced by models in the second GABLS experiment. The TKE produced by the Bélair scheme here differs significantly from the TKE produced by the same scheme in the second GABLS experiment. These differences are most pronounced when observing the maximum TKE; the maximum TKE here

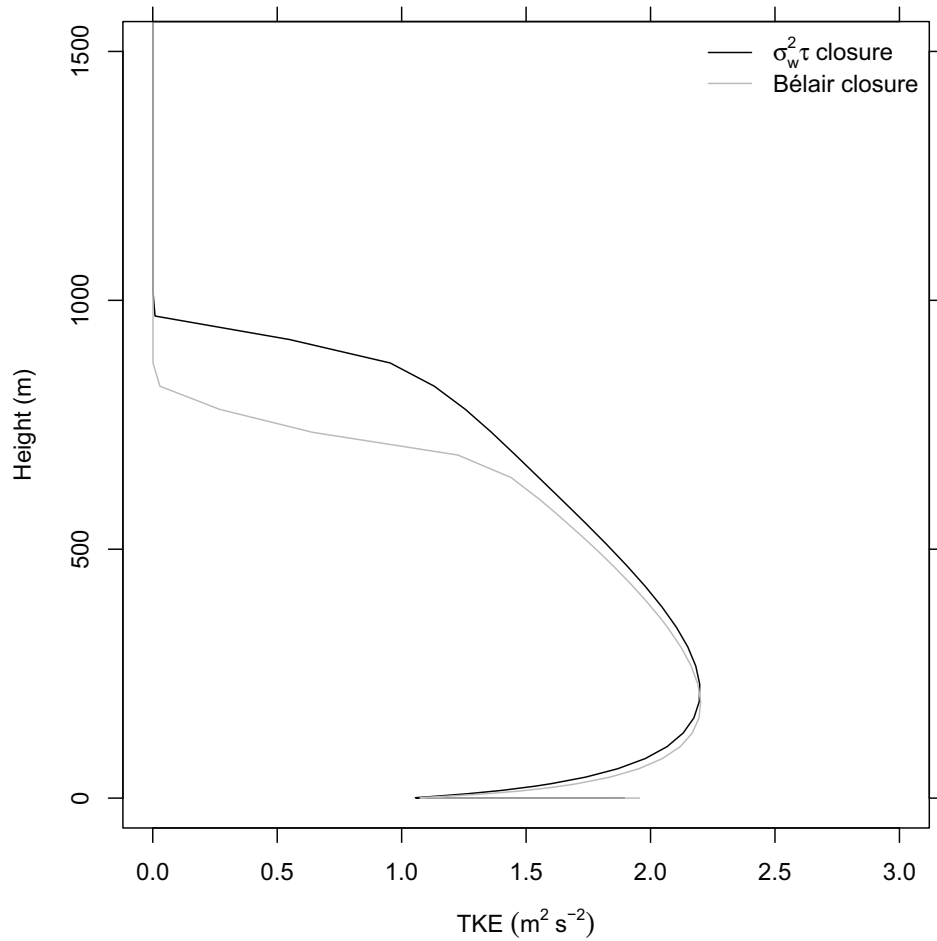


Figure 6.11: TKE model profiles for October 23, 14:00 LT; 22 hours after initialization

is nearly twice as large as that is which was reported for the Bélair et al. closure in the second GABLS experiment. This again is likely the result of differing grids as the results produced by a coarser grid (not shown) are more comparable to the results presented by Svensson et al. (2011).

7 Discussion

The second GABLS experiment has provided an appropriate and easily implementable test for the $\sigma_w^2 - \tau_w$ model (Wilson, 2012), which was built upon Durbin's (1991) formulation for eddy viscosity. However, the simple prescription of surface temperature and the limiting of geostrophic winds to constant values must be kept in mind when comparing model results to observations. Nevertheless, even with these limitations (which are largely the result of simplified initial and boundary conditions in the experimental design), the $\sigma_w^2 - \tau_w$ scheme generally performed well, certainly no worse than the general results presented by Svensson et al. (2011).

As seen in Figure 6.1, the temperatures for the late evening and early morning the first night, as well as the temperatures the entire evening the second night, are higher than those observed. These elevated temperatures are consistent with the results produced by many of the models as found in the second GABLS experiment (not shown), which is likely the result of deviations between actual surface temperature measurements and model forcing. The prescribed surface temperatures are assigned as either a linear or sinusoidal function of time (see Table 5.3), and deviations between prescribed surface temperature and measurements occur particularly during the second half of the experiment (see Svensson et al. 2011, Figure 1). It should be noted, as mentioned by Svensson et al. (2011), that the driving surface temperature may have been implemented differently among different models as the instructions regarding the specification of surface temperature were open to interpretation, i.e., a "skin" temperature was given as a function of time without specific instructions regarding the boundary conditions or implementation level. This could result in inconsistencies between results presented here and results for all models presented in the second GABLS experiment. Similarly, the coarse resolution used by some models in the second GABLS experiment may account for some discrepancy as well.

One of the greatest discrepancies between expected results and those provided by the $\sigma_w^2 - \tau_w$ model occur during the late morning, early afternoon, on October 23. As shown in Figures 6.2, 6.3, 6.4, 6.6 and 6.7, the $\sigma_w^2 - \tau_w$ model illustrates: a delay in the downward transfer of momentum, a slow increase in sensible heat flux as the surface warms, a slow increase in friction

velocity, and a slow increase in production of TKE and vertical velocity variance during the onset of convective mixing in the morning. The $\sigma_w^2 - \tau_w$ model does show a rapid increase in wind speed as surface heating begins (as one would expect), however, it does not increase to the observed wind speed, nor are the higher wind speeds sustained as the wind speed surprisingly decreases mid morning before increasing again around noon local time. As surface heating begins, the surface inversion is not being eroded quickly enough to allow the downward transfer of momentum from above the ABL to the surface (see Figures 7.1a-7.1e). This implies not enough mixing may be occurring which must be the result of deficiencies in σ_w^2 and or τ_w . As seen in Figure 6.7, modeled velocity variance is less than half of that found in observations during for this time period, so one can suspect the fault lies in velocity variance, although it remains to be proven whether this is the result of forcing or a deficiency in the model. Wilson (2012) found the Bélair scheme performed better than the $\sigma_w^2 - \tau_w$ closure when comparing model erosion of an inversion aloft (within the entrainment zone) suggesting refinements may be needed to latter scheme.

Interestingly, these general results were also seen in the second GABLS experiment among many of the TKE models whose lowest grid point was less than 5 m (see Figures 4, 5, 6, and 8 in Svensson et al. (2011)). In regards to wind speed specifically, similar results are also seen in several of the TKE models where the lowest grid point was greater than 5 m (including the Bélair scheme – this is also evident in the Bélair results presented here, albeit to a lesser extent) and is even evident in several first-order schemes. This indicates the under production of turbulence in general by most models, which begins during the transition from stable to unstable atmospheric conditions, and results in less mixing that is sustained throughout the afternoon.

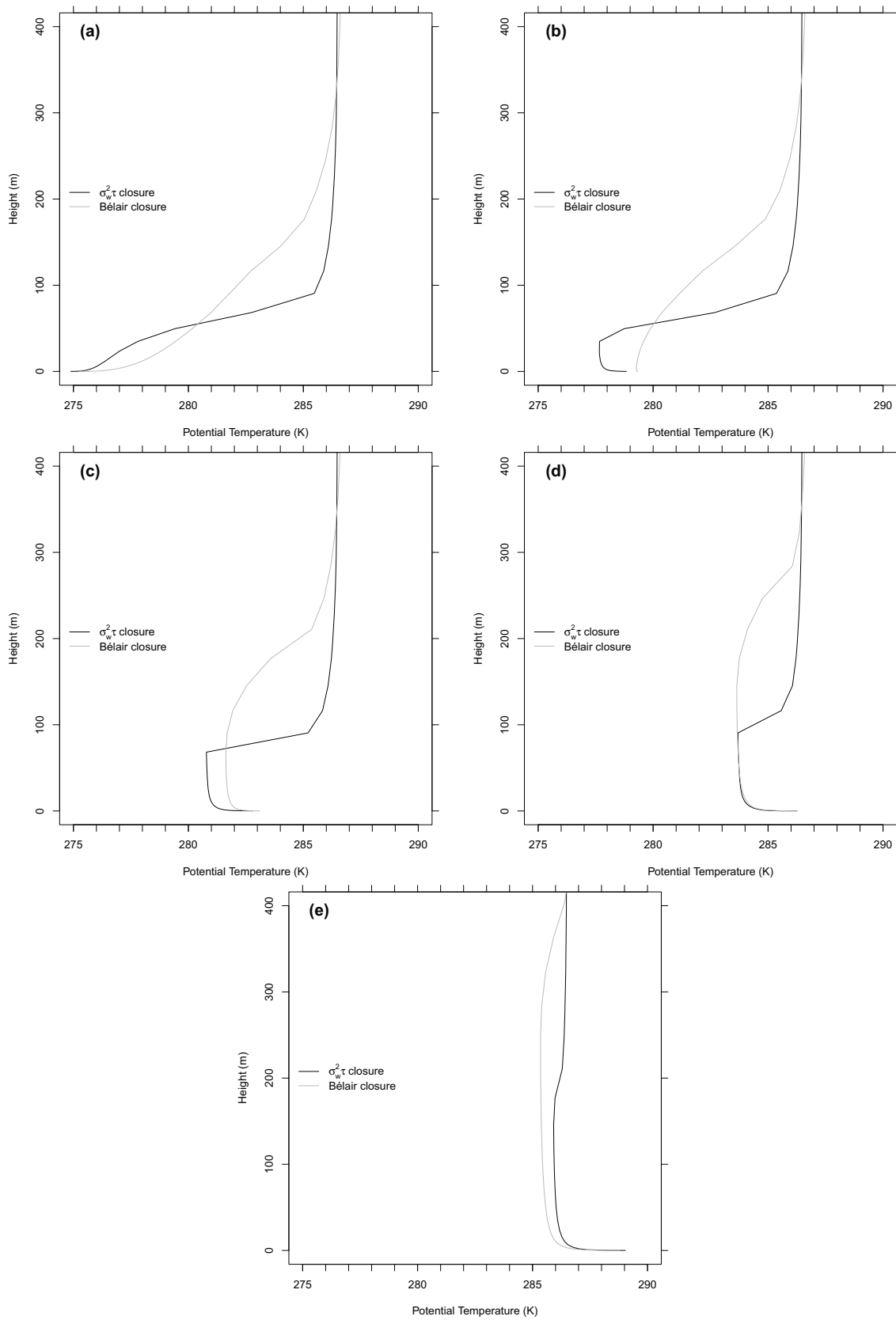


Figure 7.1: Near surface potential temperature profiles for the $\sigma_w^2 - \tau_w$ and Bélair schemes on October 23; (a) 08:00 LT (b) 09:00 LT (c) 10:00 LT (d) 11:00 LT (e) 12:00 LT

As seen in Figure 6.6 above, neither model produces enough TKE when compared to the observations, and similarly in Figure 6.7, the $\sigma_w^2 - \tau_w$ closure does not produce enough vertical velocity variance during the turbulent afternoon. TKE models in the second GABLS experiment generally do not produce enough TKE during this time either. It is possible, however, that these results could be due to forcing that is not strong enough, although there are several models in the second GABLS experiment that do not illustrate these results, particularly first-order models with the lowest grid-point above 5 m.

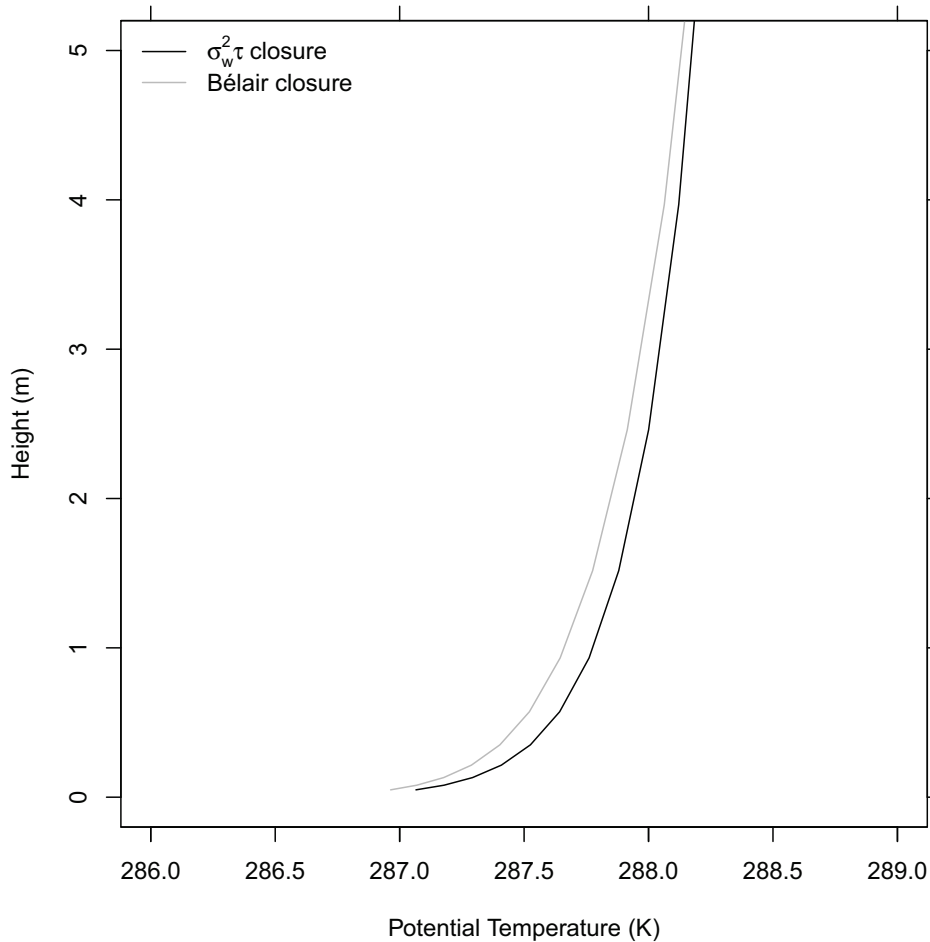


Figure 7.2: Potential temperature on October 23 at 18:00 LT

As late afternoon cooling begins and the turbulent mixed layer should transition to a residual layer, the $\sigma_w^2 - \tau_w$ model shows slower decreases in wind speed, friction velocity, the drag coefficient and vertical velocity variance than those observed. This also occurs for some models in the second GABLS experiment. In combination with the delayed increase in wind speed

and turbulence during the onset of convection, these results suggest that the model may not be responding quickly enough to changes in the forcing. A closer inspection of the potential temperature profiles (Figure 7.2) reveals that the Bélair closure is cooler and becomes stable more quickly than the $\sigma_w^2 - \tau_w$ closure during this transition from the turbulent afternoon to stable evening.

Unfortunately, there is only one morning of observations used for comparison in this experiment, so it is unknown whether these deficiencies are a general outcome during surface heating/cooling, or whether they are isolated to this particular event. Since these results are also observed within model output for several of the TKE schemes in the second GABLS experiment, these problems are likely not isolated to the $\sigma_w^2 - \tau_w$ scheme, however, further rigorous testing of the scheme is required.

There are several aspects of the Bélair scheme (which is used for comparison) that must be discussed. First, it is worth noting that using the same grid as the $\sigma_w^2 - \tau_w$ closure (i.e., 100 grid points which are log linearly distributed) the Bélair scheme became unstable shortly after hour 51. This instability did not occur with the $\sigma_w^2 - \tau_w$ scheme. The instability arose at the location where the prescribed mean vertical velocity began to decrease toward the surface (the uppermost level of convergence, see Equation 5.1). At this point (roughly 930 to 1000 m above the surface) the atmosphere was very stable, however a shallow and weakly unstable layer developed which caused the Richardson number to fall below zero affecting eddy diffusivity (see Equations 4.10-4.14). This led to numerical instability in the model. As this level was well above the atmospheric boundary layer and in order to continue the (high resolution) Bélair simulation for the remainder of the test period, the model was forced to remain stable. To achieve this, a Richardson number of 0.5 was imposed so that it remained consistent with surrounding grid points and the TKE also was forced to remain at its minimum (again, to ensure consistency with all surrounding grid points). This provided stability in the model and should not have affected results within the atmospheric boundary layer as this shallow layer of instability was located far above the ABL for the remainder of the evening until the model test was completed.

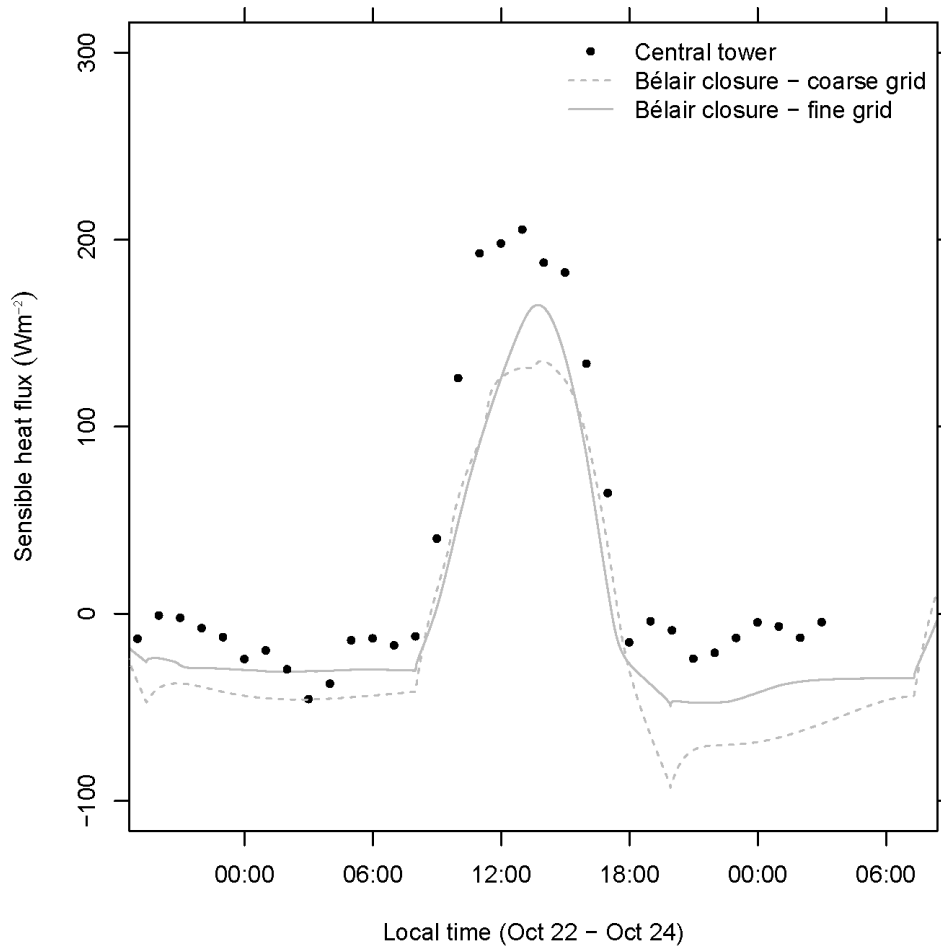


Figure 7.3: Sensible heat flux time series for the Bélair scheme using two different grids

Second, the Bélair scheme for the second GABLS experiment was run using the MSC model (as described by Svensson et al. 2011). It is assumed that this is the Meteorological Service of Canada’s model which is an operational model. Svensson et al. (2011) does not provide the distribution of grid points for each model, however it is noted that the bottom grid point is located at approximately 25 m AGL for the Bélair scheme with 21 grid points below 1000 m. This implies a relatively coarse grid which may explain why the results presented here differ from the results presented in the second GABLS experiment for the Bélair scheme (particularly for the sensible heat flux, the potential temperature profile on October 23, and the TKE profile). When reducing the number of grid points and setting the lowest grid point elevation above 5

¹⁶Running the Bélair scheme with a coarse resolution did not require intervention to ensure numerical stability.

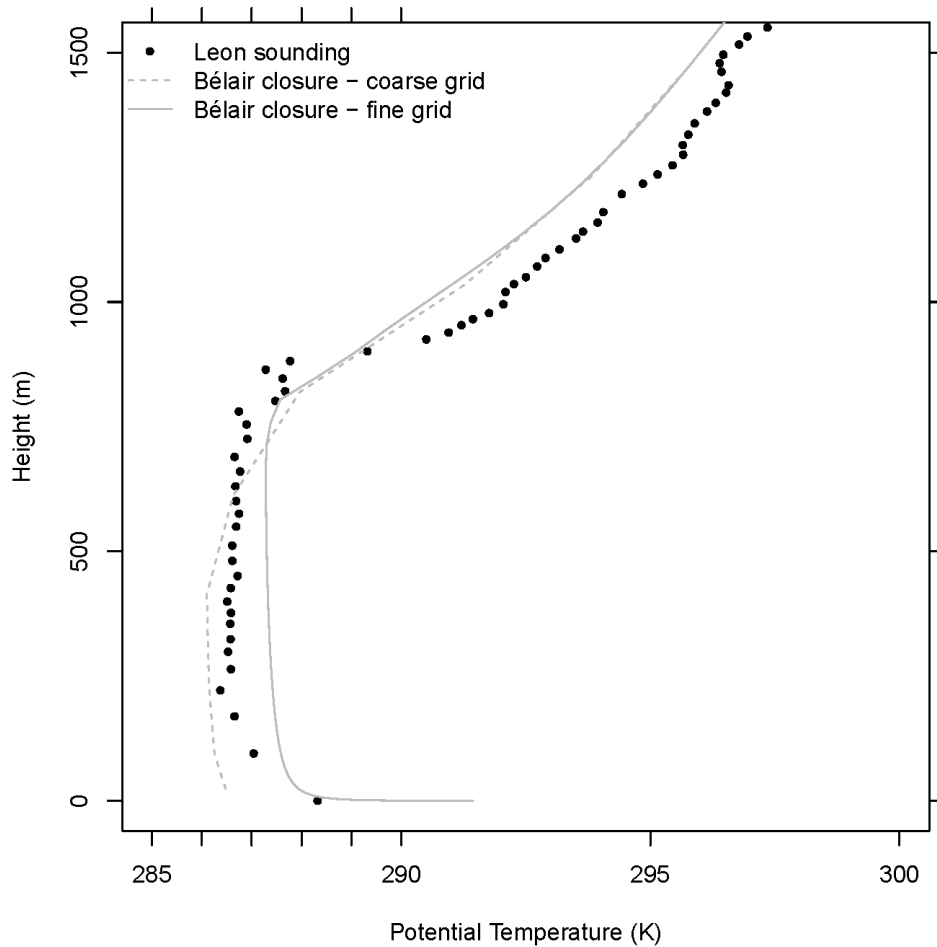


Figure 7.4: Potential temperature profile for the Bélair scheme using two different grids for October 23,14:00 LT

those presented by Svensson et al. (2011) for the Bélair scheme.

Figure 7.3 shows the results for the Bélair scheme using the fine grid presented above as well as results using a coarse grid. In the results using a coarse grid, the bottom grid point for temperature, wind and humidity was located approximately 20 m above ground and the model contained only 20 grid points over the entire domain. Since potential temperature and wind speed vary with height one will not obtain consistent fluxes using grid points that vary over several meters (or in this case tens of meters). Also, when reducing the number of grid points (i.e., increasing the space between grid points) the model may not be able to accurately capture smaller scale features that must be modeled in order to obtain accurate results. The differences between solutions given different grids is also evident in Figure 7.4. Here the potential tempera-

ture using the coarse grid is much closer to the results of the Bélair scheme as cited by Svensson et al. (2011), where the potential temperature profile was consistently cooler (close to the surface it was more than 1°C cooler) than the observations for the entire ABL. Since the Meteorological Service of Canada runs an operational model, it is not surprising that their simulation of the test case using the Bélair closure would differ from the results presented here, based on an implementation that has incorporated a much higher resolution.

8 Further Research

As this experiment was conducted for only one full diurnal cycle one cannot suggest that the successes or failures of the model are conclusive regarding model utility. When comparing the alternative scheme's performance to the second GABLS experiment, the proposed model produces results similar to those generally found by Svensson et al. (2011). However, some results suggest the model may have trouble eroding a temperature inversion fast enough, as shown in the results presented in this thesis work, as well as results presented by Wilson (2012). As only two experiments have been conducted to evaluate the proposed scheme, further research is required. A more comprehensive examination of the delay in inversion erosion through additional experiments may help to determine if adjustments need to be made to formulations controlling σ_w^2 and or τ_w . Furthermore, as it remains uncertain whether inaccurate model forcing contributed to discrepancies between observations and model output, additional experiments conducted over at least a full diurnal cycle with well represented forcing conditions should be conducted.

9 Conclusion

The purpose of this research has been to evaluate the ABL closure adopted by Wilson (2012) against a range of alternative closures by performing a model inter-comparison through a strictly controlled test (Svensson et al., 2011). This controlled test was developed from observations taken on October 22, 1999 during the CASES-99 study which provide initial and boundary conditions for the model run. The test required a 59 hour simulation of atmospheric conditions driven by prescribed surface temperature, subsidence and constant geostrophic wind speed. The closure tested incorporates an alternative scheme that parameterizes eddy viscosity in terms of (strictly) vertical motion, contrasting with more usual schemes which parametrize eddy viscosity as a function of TKE (which which quantifies the kinetic energy contributed by horizontal as well as vertical transport). This closure scheme was also tested alongside a well known TKE closure scheme developed by Bélair et al. (1999).

Judged from the perspective of the ensemble of outcomes (from many models) relative to the observations, and bearing in mind some uncertainties relative to the latter, the $\sigma_w^2 - \tau_w$ model performed adequately. The discrepancies between model forcing and actual conditions may explain some of the variations seen between model results and observations. The greatest discrepancy is found during the morning after sunrise and before noon when the temperature inversion should be burning out as instability increases. During this time the $\sigma_w^2 - \tau_w$ closure does not produce enough turbulence, however, this behavior is not limited to this particular model and its results as presented here; Svensson et al. (2011) also reports that many of the models tested in the second GABLS experiment provide similar results. Hence, further examination into the forcing conditions is required to determine whether the anomalous results are due to model deficiency or discrepancies between model forcing and actual conditions at the site. This experiment only provided one full diurnal cycle for comparison and thus further testing over various stability conditions is required.

References

- G. Alfonsi. Reynolds-averaged Navier-Stokes equations for turbulence modeling. *Applied Mechanics Reviews*, 62:040802 1–20, 2009.
- D. D. Apsley and I. P. Castro. A limited-length-scale k- model for the neutral and stably-stratified atmospheric boundary layer. *Boundary-Layer Meteorology*, 83(1):75–98, 1997.
- S.P. Arya. *Introduction to Micrometeorology*. International Geophysics Series. Academic Press, 1988. ISBN 9780120644902.
- S.P. Arya. Micrometeorology and atmospheric boundary layer. *Pure and Applied Geophysics*, 162(10):1721–1745, 2005. ISSN 0033-4553. doi: 10.1007/s00024-005-2690-y.
- S. Bélair, J. Mailhot, J. W. Strapp, and J. I. Macpherson. An examination of local versus nonlocal aspects of a TKE-based boundary layer scheme in clear convective conditions. *Journal of Applied Meteorology*, 38(10):1499–1518, 1999.
- R. Benoit, J. Cote, and J. Mailhot. Inclusion of a TKE boundary layer parameterization in the Canadian regional finite-element model. *Monthly Weather Review*, 117(8):1726–1750, 1989.
- A. K. Blackadar. The vertical distribution of wind and turbulent exchange in a neutral atmosphere. *Journal of Geophysical Research*, 67:3095–3102, 1962.
- A. K. Blackadar. *Turbulence and Diffusion in the Atmosphere: Lectures in Environmental Sciences*. Springer Berlin Heidelberg, 1997.
- P. Bougeault and P. Lacarrere. Parameterization of orography-induced turbulence in a mesobeta-scale model. *Monthly Weather Review*, 117(8):1872–1890, 1989.
- R. H. Clarke, A. J. Dyer, R. R. Brook, D. G. Reid, and A. J. Troup. The Wangara experiment: Boundary layer data. Technical report, Commonwealth Scientific and Industrial Research Organization, 1971.

- J. Côté, S. Gravel, A. Méthot, A. Patoine, M. Roch, and A. Staniforth. The operational CMC-MRB global environmental multiscale (GEM) model. Part I: Design considerations and formulation. *Monthly Weather Review*, 126(6):1373–1395, 1998.
- J. Cuxart, A. A. M. Holtslag, R. J. Beare, E. Bazile, A. Beljaars, A. Cheng, L. Conangla, M. Ek, F. Freedman, R. Hamdi, A. Kerstein, H. Kitagawa, G. Lenderink, D. Lewellen, J. Mailhot, T. Mauritsen, V. Perov, G. Schayes, G. . Steeneveld, G. Svensson, P. Taylor, W. Weng, S. Wunsch, and K. . Xu. Single-column model intercomparison for a stably stratified atmospheric boundary layer. *Boundary-Layer Meteorology*, 118(2):273–303, 2006.
- Y. Delage. A numerical study of the nocturnal atmospheric boundary layer. *Quarterly Journal of the Royal Meteorological Society*, 100(425):351–364, 1974.
- P. A. Durbin. Near-wall turbulence closure modeling without "damping functions". *Theoretical and Computational Fluid Dynamics*, 3(1):1–13, 1991.
- A. J. Dyer and E. F. Bradley. An alternative analysis of flux-gradient relationships at the 1976 ITCE. *Boundary-Layer Meteorology*, 22(1):3–19, 1982.
- V. W. Ekman. On the influence of the Earth's rotation on ocean currents. *Arkiv För Matematic, Astronomi Och Fysik*, 2(11):1–52, 1905.
- J. R. Garratt. *The atmospheric boundary layer*. Cambridge University Press, 1992. ISBN 0521380529.
- S. Ghosal and P. Moin. The basic equations for the large eddy simulation of turbulent flows in complex geometry. *Journal of Computational Physics*, 118(1):24–37, 1995.
- G. D. Hess and J. R. Garratt. Evaluating models of the neutral, barotropic planetary boundary layer using integral measures: Part II. Modelling observed conditions. *Boundary-Layer Meteorology*, 104(3):359–369, 2002.

- G. D. Hess, B. B. Hicks, and T. Yamada. The impact of the Wangara experiment. *Boundary-Layer Meteorology*, 20(2):135–174, 1981.
- T. Holt and S. Raman. A review and comparative evaluation of multilevel boundary layer parameterizations for first-order and turbulent kinetic energy closure schemes. *Reviews of Geophysics*, 26(4):761–780, 1988.
- W. P. Jones and B. E. Launder. The prediction of laminarization with a two-equation model of turbulence. *International Journal of Heat and Mass Transfer*, 15(2):301–314, 1972.
- J. Mailhot and R. Benoit. A finite-element model of the atmospheric boundary layer suitable for use with numerical weather prediction models. *Journal of the Atmospheric Sciences*, 39(10):2249–2266, 1982.
- J. Mailhot, S. Bélair, R. Benoit, B. Bilodeau, Y. Delage, L. Fillion, L. Garand, C. Girard, and A. Tremblay. Scientific description of RPN physics library - version 3.6, 1998a. URL <http://collaboration.cmc.ec.gc.ca/science/rpn/physics/physic98.pdf>.
- J. Mailhot, J. W. Strapp, J. I. MacPherson, R. Benoit, S. Blair, N. R. Donaldson, F. Fraude, M. Benjamin, I. Zawadzki, and R. R. Rogers. The Montreal-96 experiment on regional mixing and ozone (MERMOSZ): An overview and some preliminary results. *Bulletin of the American Meteorological Society*, 79(3):433–442, 1998b.
- S. Marlatt, S. Waggy, and S. Biringen. Direct numerical simulation of the turbulent Ekman layer: Evaluation of closure models. *Journal of the Atmospheric Sciences*, 69(3):1106–1117, 2012.
- G. L. Mellor and T. Yamada. A hierarchy of turbulence closure models for planetary boundary layers. *Journal of Atmospheric Science*, 31:1791–1806, 1974.
- A. S. Monin and A. M. Yaglom. *Statistical fluid mechanics*. MIT Press, Cambridge, Massachusetts, 1971. ISBN 0262130629.

- J. J. O'Brien. A note on the vertical structure of the eddy exchange coefficient in the planetary boundary layer. *Journal of Atmospheric Science*, 27:1213–1215, 1970.
- A. Peña, S.-E. Gryning, and J. Mann. On the length-scale of the wind profile. *Quarterly Journal of the Royal Meteorological Society*, 136(653):2119–2131, 2010.
- S. Pope. *Turbulent Flows*. Cambridge University Press, 2000. ISBN 0521591252.
- G. S. Poulos, W. Blumen, D. C. Fritts, J. K. Lundquist, J. Sun, S. P. Burns, C. Nappo, R. Banta, R. Newsom, J. Cuxart, E. Terradellas, B. Balsley, and M. Jensen. CASES-99: A comprehensive investigation of the stable nocturnal boundary layer. *Bulletin of the American Meteorological Society*, 83(4):555–581, 2002.
- R Development Core Team. R: A language and environment for statistical computing, 2007. URL www.r-project.org.
- P. Schotanus, F. T. M. Nieuwstadt, and H. A. R. De Bruin. Temperature measurement with a sonic anemometer and its application to heat and moisture fluxes. *Boundary-Layer Meteorology*, 26(1):81–93, 1983.
- R. B. Stull. *An Introduction to Boundary Layer Meteorology*. Kluwer Academic Publishers, 1988. ISBN 90-277-2768-6.
- G. Svensson, A. A. M. Holtslag, V. Kumar, T. Mauritsen, G. J. Steeneveld, W. M. Angevine, E. Bazile, A. Beljaars, E. I. F. de Bruijn, A. Cheng, L. Conangla, J. Cuxart, M. Ek, M. J. Falk, F. Freedman, H. Kitagawa, V. E. Larson, A. Lock, J. Mailhot, V. Masson, S. Park, J. Pleim, S. Söderberg, W. Weng, and M. Zampieri. Evaluation of the diurnal cycle in the atmospheric boundary layer over land as represented by a variety of single-column models: The second GABLS experiment. *Boundary-Layer Meteorology*, 140(2):177–206, 2011.
- W. C. Swinbank. The exponential wind profile. *Quarterly Journal of the Royal Meteorological Society*, 90:119–135, 1964.

- G. I. Taylor. Diffusion by continuous movements. *Proceedings of the London Mathematical Society*, 20:196–211, 1921.
- G. Therry and P. Lacarrère. Improving the eddy kinetic energy model for planetary boundary layer description. *Boundary-Layer Meteorology*, 25(1):63–88, 1983.
- A. M. Thomkins, P. Bechtold, A. C. M. Beljaars, A. Benedetti, S. Cheinet, M. Janisková, M. Köhler, P. Lopez, and J.-J. Morcrette. Moist physical processes in the IFS: progress and plans. Technical report, European Centre for Medium-Range Weather Forecasts, 2004.
- E. K. Webb, G. I. Pearman, and R. Leuning. Correction of flux measurements for density effects due to heat and water vapour transfer. *Quarterly Journal Royal Meteorological Society*, 106(447):85–100, 1980.
- W. Weng and P. A. Taylor. On modelling the one-dimensional atmospheric boundary layer. *Boundary-Layer Meteorology*, 107(2):371–400, 2003.
- J. D. Wilson. An alternative eddy-viscosity model for the horizontally uniform atmospheric boundary layer. *Boundary-Layer Meteorology*, 145(1):165–184, 2012.
- D. Xu and P. A. Taylor. An $E - \epsilon - l$ turbulence closure scheme for planetary boundary-layer models: The neutrally stratified case. *Boundary-Layer Meteorology*, 84(2):247–266, 1997.
- T. Yamada. Simulations of nocturnal drainage flows by a q^2 turbulence closure model. *Journal of the Atmospheric Sciences*, 40(1):91–106, 1983.

Appendix A Model Surface Layer - Kerang Simulations

As discussed in Section 5.2.2, the surface layer is not modeled using MOST explicitly; instead, the model inherently (and by design) produces surface layer profiles consistent with MOST, as illustrated here by a comparison with observations taken during the Kerang boundary layer experiment and MOST profiles (Figures A.1a, A.1b and A.1c)¹⁷. The Kerang boundary layer experiment was conducted near Kerang, Australia in February 1962 (Swinbank, 1964). The observations shown are taken from run 47 of the said experiment for mean wind speed, temperature and specific humidity. The surface pressure was 1000 mb. The friction velocity and temperature scales are 0.34 ms^{-1} and -0.34 K , respectively, as determined by fitting MOST profiles to the observations at 1 m (see Appendix D for further details on fitting MOST profiles to observations). The Obukhov length and surface heat flux are then respectively -25 m and 0.116 m K s^{-1} , and the roughness length is 0.0053 m based on the lowest wind speed measurement, the friction velocity and Obukhov length determined from the MOST profile best fit. The model was driven by measured surface fluxes of latent and sensible heat, and after every iteration the profiles of wind, temperature and specific humidity were adjusted to match observed values at a single reference height (1 m for all properties). The wind profile was adjusted multiplicatively and potential temperature and specific humidity profiles were adjusted additively, i.e., the entire wind speed profile was multiplied by the percent discrepancy between the observation and modeled wind speed at the observation height, and the temperature and humidity profiles were adjusted by adding the discrepancy between the observed and modeled temperature and specific humidity respectively. The friction velocity and temperature scales from the model are 0.35 ms^{-1} and -0.34 K .

Figures A.1a, A.1b and A.1c illustrate model results compared to observations and MOST profiles for the Kerang boundary layer experiment. Temperature and wind speed are consistent between the model, MOST and observations. Specific humidity model results are consistent

¹⁷These surface layer simulations and MO fitted profiles were run by Dr. John Wilson and the data, as shown in the figures, was provided via personal communication.

with MOST fitted profiles, although observations show slightly more water vapor at 16 m than is predicted by the model and the MOST profile.

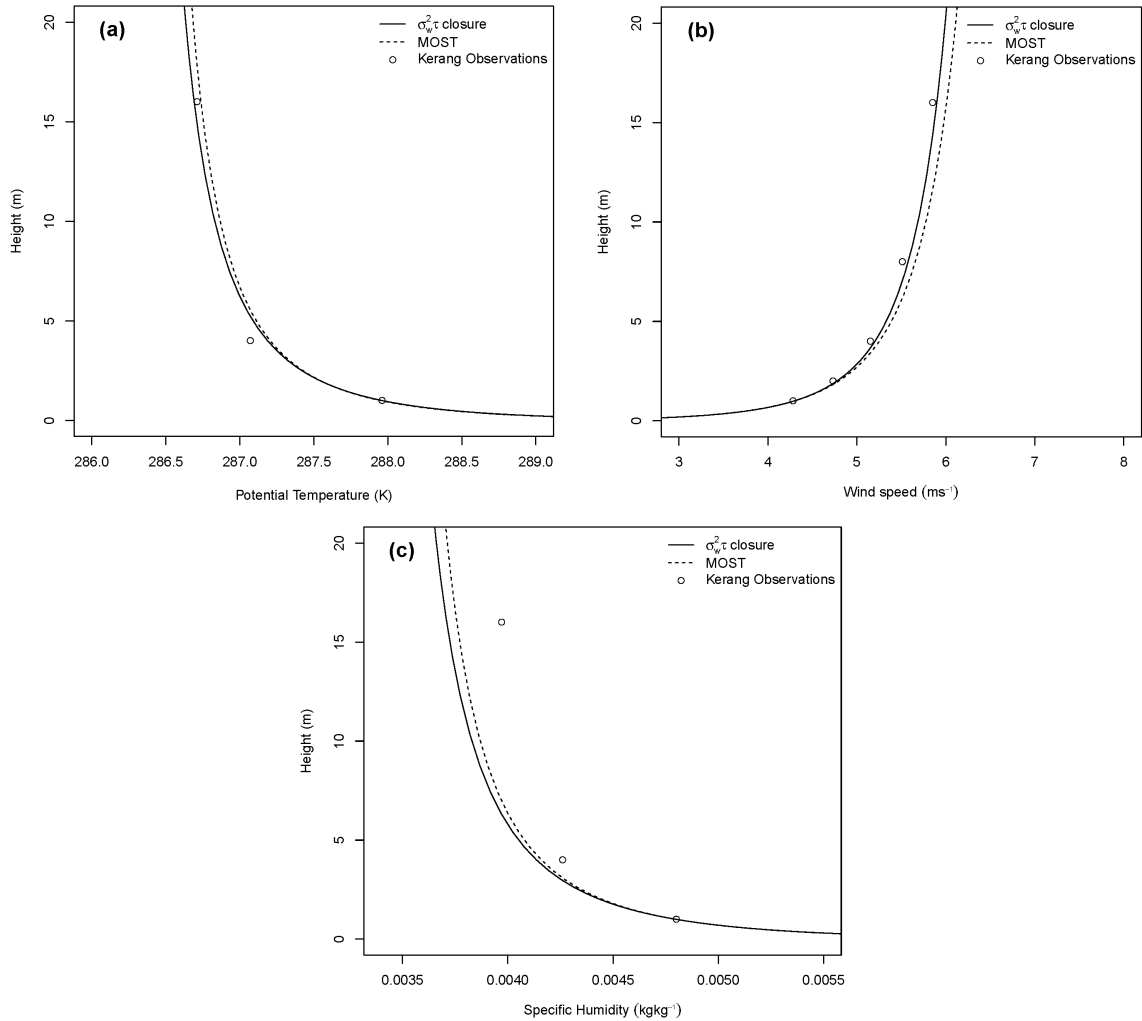


Figure A.1: Surface layer profiles as produced by the model, MOST and observations taken during the Kerang surface layer experiment; (a) Potential temperature (b) Wind speed (c) Specific humidity. Note: the model is forced to fit the observations at a single level, viz. $z=1$ m.

Appendix B Model Surface Drag

As surface drag, S , is necessary for boundary conditions within the model, it is incorporated into the zonal and meridional velocity equations at the lowest grid point such that it acts in the opposite direction of the wind. Surface drag is parameterized (for zonal velocity as example) by computing its zonal component,

$$S_u = u_*^2 \cos \alpha = u_*^2 \frac{u}{\sqrt{u^2 + v^2}} \quad (\text{B.1})$$

where α is the angle of the wind direction. Since

$$u(z) = u_* \frac{\cos \alpha}{k_v} \ln \frac{z}{z_0} \quad (\text{B.2})$$

and

$$v(z) = u_* \frac{\sin \alpha}{k_v} \ln \frac{z}{z_0}, \quad (\text{B.3})$$

one can then formulate

$$u_*^2 = C_D (u^2 + v^2) \quad (\text{B.4})$$

using equation 5.33. Substituting Equation B.4 into Equation B.1, we thus find the zonal component of surface drag to be

$$S_u = C_D u_1 \sqrt{u_1^2 + v_1^2}, \quad (\text{B.5})$$

where u_1 is the model's zonal wind speed at the lowest gridpoint.

Appendix C WPL and Schotanus Corrections

The Webb, Pearman and Leuning correction (WPL correction) is required when measuring fluxes of water vapor (or CO₂) in the atmosphere via eddy covariance or mean gradient techniques (Webb et al., 1980). The need for this correction arises due to the variations in density which are the result of a heat or vapor flux. Webb et al. (1980) derives the correction for water vapor:

$$E = (1 + \mu\sigma) \left(\overline{w'\rho'_v} + \frac{\overline{\rho_v}}{\overline{T}} \overline{w'T'} \right) \quad (\text{C.1})$$

where E is the corrected water vapor flux, μ is the ratio of molecular mass for dry air to the molecular mass of water vapor, σ is the ratio of water vapor density to dry air density, $\overline{w'\rho'_v}$ is the uncorrected water vapor flux and $\overline{\rho_v}$ is the mean water vapor density. This correction is applied in conjunction with the Schotanus correction (Schotanus et al., 1983) for temperature.

The Schotanus temperature correction is needed as temperature is derived from the anemometer measured speed of sound, and velocity is dependent on water vapor content and temperature. As derived by Schotanus et al. (1983) the temperature correction is:

$$\overline{T} = \frac{\overline{T_s}}{1 + 0.51\overline{Q}} \quad (\text{C.2})$$

where $\overline{T_s}$ is the mean uncorrected temperature and \overline{Q} is the mean specific humidity in kgkg⁻¹. Similarly they derive a correction for the measured temperature fluctuation,

$$T' = T'_s - 0.51Q'\overline{T} \quad (\text{C.3})$$

where T'_s is the uncorrected temperature fluctuation.

As previously discussed, the Schotanus and WPL corrections are implemented iteratively until both the corrected water vapor fluxes and the corrected temperatures converge.

Appendix D Monin Obukhov Similarity Theory Profiles

The Monin-Obukhov profiles that were fitted to the data were obtained by comparing each member of an ensemble of computed profiles, covering all combinations of u_* and T_* , within a reasonable range, to the tower data (recall that the slopes of the MO wind and temperature profiles are directly proportional to the key scales u_* and T_* , and in effect one is attempting to find the unique combination (u_*T_*) that results in a best accord of the theoretical and measured profiles). The velocity and temperature scales were optimized through the minimization of the residual

$$R = \frac{\sum_1^N (\Delta U_{meas} - \Delta U_{theor})^2}{\delta U^2} + \frac{\sum_1^N (\Delta T_{meas} - \Delta T_{theor})^2}{\delta T^2} \quad (\text{D.1})$$

where N is one less than the number of measurement heights on the tower, ΔU_{meas} is the difference in wind speed between the reference level and a sonic anemometer above, ΔU_{theor} is the theoretical wind speed difference between the reference height and a sonic anemometer above using MOST and a combination of u_* and T_* , δU^2 is a rough specification of instrumental uncertainty, ΔT_{meas} is the difference in temperature between the reference level and a sonic anemometer above, ΔT_{theor} is the theoretical temperature difference between the reference height and a sonic anemometer above using MOST and a combination of u_* and T_* (the same as for ΔU_{theor}) and δT^2 is the instrument temperature uncertainty. Once the optimal combination of u_* and T_* were obtained, the optimization procedure was performed again for a physically realistic range of values for q_* in order to obtain a fitted profile for specific humidity.

The theoretical profiles for wind speed differences were calculated based on the Obukhov length (a stability parameter), L , and were computed according to Dyer and Bradley (1982) such that:

$$U(z) - U(z_{ref}) = \begin{cases} \frac{u_*}{k_v} \left[\ln \frac{z}{z_{ref}} - \Psi_m \left(\frac{z}{L} \right) + \Psi_m \left(\frac{z_{ref}}{L} \right) \right] & \text{if } L < 0 \\ \frac{u_*}{k_v} \left[\ln \frac{z}{z_{ref}} + 5 \frac{z - z_{ref}}{L} \right] & \text{if } L \geq 0 \end{cases} \quad (\text{D.2})$$

where

$$\Psi_m \left(\frac{z}{L} \right) = 2 \ln \left(\frac{1 + \phi_m^{-1}}{2} \right) + \ln \left(\frac{1 + \phi_m^{-2}}{2} \right) - 2 \arctan(\phi_m^{-1}) + \frac{\pi}{2} \quad (\text{D.3})$$

and

$$\phi_m = \left(1 - 28 \frac{z}{L} \right)^{-\frac{1}{4}}. \quad (\text{D.4})$$

Similarly, the theoretical profiles for temperature differences (and specific humidity) were calculated as:

$$T(z) - T(z_{ref}) = \begin{cases} \frac{t_*}{k_v} \left[\ln \frac{z}{z_{ref}} - \Psi_h \left(\frac{z}{L} \right) + \Psi_h \left(\frac{z_{ref}}{L} \right) \right] & \text{if } L < 0 \\ \frac{t_*}{k_v} \left[\ln \frac{z}{z_{ref}} + 5 \frac{z - z_{ref}}{L} \right] & \text{if } L \geq 0 \end{cases} \quad (\text{D.5})$$

where

$$\Psi_h \left(\frac{z}{L} \right) = 2 \ln \left[\frac{1 + \phi_h^{-1}}{2} \right] \quad (\text{D.6})$$

and

$$\phi_h = \left(1 - 14 \frac{z}{L} \right)^{-\frac{1}{2}}. \quad (\text{D.7})$$

To reconcile discrepancies between data and fitted profiles (for the stable ABL in particular) MO profiles were only fitted for heights below $3L$. Initial plots of data versus fitted functions illustrated unacceptable fits during strong stability (see Figure D.1a), therefore it became necessary to limit the data that was included in the profile fitting process. When the ABL is extremely stable, the surface layer can become shallow; as such, limiting the data for fitting below $3L$ reduced the number of measurements available, but ensured that the profiles were fitted ONLY within the surface layer. This was achieved by first calculating the value of $3L$ for all combinations of u_* and t_* . Next, the residual was calculated using only tower data below the potential $3L$, and finally, the minimum residual was found and the unique pair of scales were used to approximate the unknowns. After the modified fitting process was performed, the new MO profile fit the surface layer data well (see Figure D.1b).

The minimum value of $3L$ for the period examined remained above 5 m. Values of $3L$ just

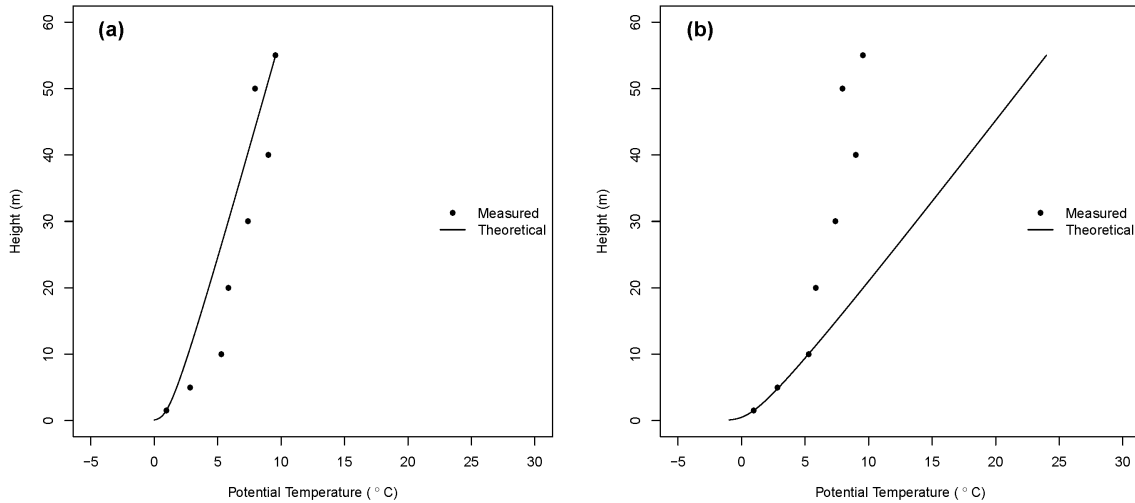


Figure D.1: Potential temperature and fitted MO profiles for October 24 02:25 LT; (a) all tower data used to fit MO profiles; $L=9.6$ m and (b) all tower data less than $3L$ used to fit MO profile; $L=6.3$ m

above 5 m resulted in reduced data available to fitting (as no tower data above the 5 m was included in the fitting process); however the interpolation was required to determine unknowns at 2 m and so the residual was always calculated using at least 2 measurements (the minimum requirement). In general, the MO profiles fit well during unstable stratification and no additional steps were needed to accurately fit the profiles (see Figure D.2).

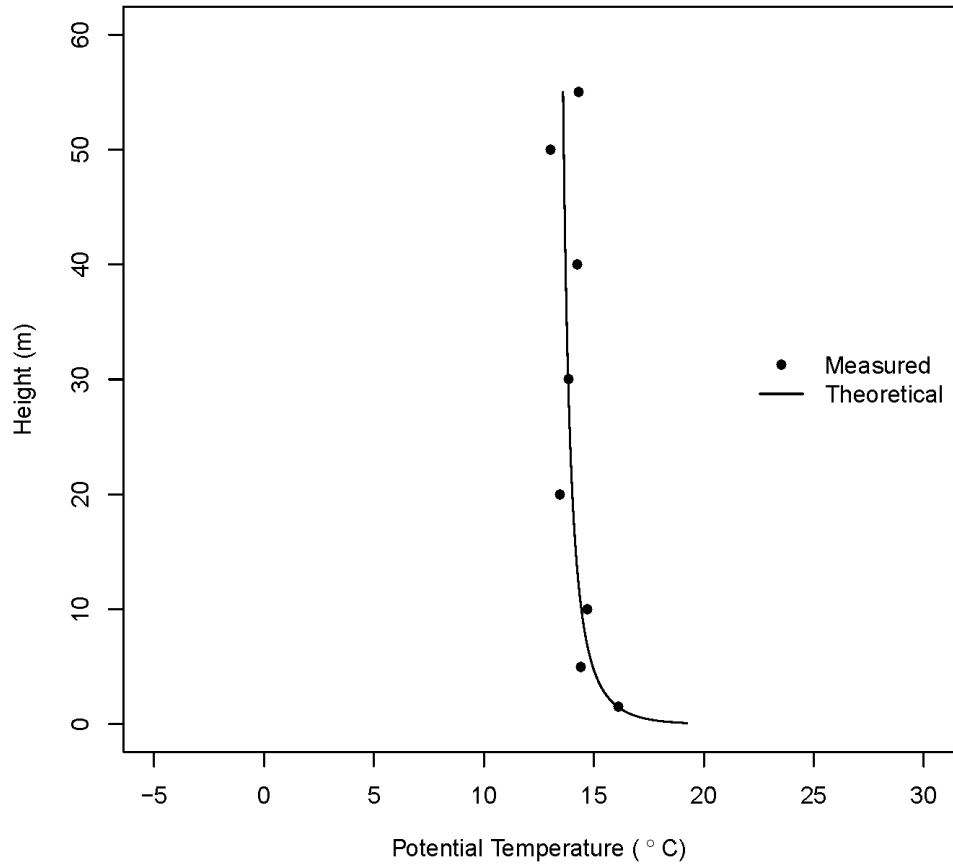


Figure D.2: Potential temperature mean measurement and fitted MO profile during unstable stratification for October 23 15:00 LT